MONTHLY NOTICES of the Royal Astronomical Society

The Reversibility Error Method (REM): a new, dynamical fast indicator for planetary dynamics

Journal:	*Monthly Notices of the Royal Astronomical Society*
Manuscript ID	Draft
Manuscript type:	Main Journal
Date Submitted by the Author:	n/a

Complete List of Authors:	Panichi, Federico; University of Szczecin, Institute of Physics and CASA*, Faculty of Mathematics and Physics Gozdziewski, Krzysztof; Centre for Astronomy, Faculty of Physics, Astronomy and Informatics, Nicolaus Copernicus University Turchetti, Giorgio; University of Bologna, Department of Physics and Astronomy

Keywords:	celestial mechanics < Astrometry and celestial mechanics, Planetary Systems, methods: numerical < Astronomical instrumentation, methods, and techniques, methods: data analysis < Astronomical instrumentation, methods, and techniques, (stars:) planetary systems < Stars

Mon. Not. R. Astron. Soc. **000**, 1–20 (2016) Printed 24 September 2016 (MN LaTeX style file v2.2)

The Reversibility Error Method (REM): a new, dynamical fast indicator for planetary dynamics

Federico Panichi[1]⋆, Krzysztof Goździewski[2]† & Giorgio Turchetti[3]‡
[1]*Institute of Physics and CASA*, Faculty of Mathematics and Physics, University of Szczecin, Wielkopolska 15, 70-451 Szczecin, Poland*
[2]*Centre for Astronomy, Faculty of Physics, Astronomy and Informatics, Nicolaus Copernicus University, Grudziadzka 5, 87-100 Toruń, Poland*
[3]*Department of Physics and Astronomy, Alma Mater Studiorum – University of Bologna, Viale Berti Pichat 6/2, 40-127 Bologna, Italy*

Accepted .... Received ...; in original form ...

ABSTRACT
We describe the Reversibility Error Method (REM) and its applications to the planetary dynamics. REM is based on *the time-reversibility analysis* of the phase-space trajectories of conservative Hamiltonian systems. The round-off errors break the time reversibility and the displacement from the initial condition, occurring when we integrate it forward and backward for the same time interval, is related to the dynamical character of the trajectory. If the motion is chaotic, in the sense of non-zero maximal Characteristic Lyapunov Exponent (mLCE), then REM increases exponentially with time, as $\exp \lambda t$, while when the motion is regular (quasi-periodic) then REM increases as a power low in time, as t^{α}, where α and λ are real coefficients. We compare the REM with a variant of mLCE, the Mean Exponential Growth factor of Nearby Orbits (MEGNO). The test set includes the restricted three body problem and five resonant planetary systems: HD 37124, Kepler-60, Kepler-36, Kepler-29 and Kepler-26. We found a very good agreement between the results of these algorithms. Moreover, numerical implementation of REM is astonishing simple, and based on solid theoretical background. The REM requires only a symplectic and time-reversible (symmetric) integrator of the equations of motion. This method is also CPU efficient. It may be particularly useful for the dynamical analysis of multiple planetary systems in the KEPLER sample, characterized by low-eccentricity orbits and relatively weak mutual interactions. As an interesting side-result, we found a possible *stable chaos* occurrence in the Kepler-29 planetary system.

Key words: chaotic indicator—*N*-body problem—stability analysis—star: Kepler-26, Kepler-29, Kepler-36, Kepler-60,HD 37124

1 INTRODUCTION

During just a few past years, the space mission KEPLER has detected more than 550 multi-planet compact systems with relatively small-mass super-Earth planets[1]. That has brought a new understanding of the orbital architectures and the long-term evolution of extrasolar systems. Short period exoplanets in multi-planet systems raise a puzzling scenario of their formation and evolution. In such near-resonant or resonant compact configurations, wide ranges of gravitational interactions between planets are expected and chaotic dynamics due to resonance overlap (Chirikov 1979; Wisdom 1983; Quillen 2011) may lead to close encounters (Chambers et al. 1996; Chatterjee et al. 2008) and self-disrupting systems (Chambers 1999). The mean motion resonances (MMRs) and secular resonances are the crucial factors for the orbital evolution of compact planetary systems and determine their long-term stability (Morbidelli 2002; Guzzo 2005; Quillen 2011).

A dynamical analysis of the observational data is often a challenge by itself. Short baseline, sparse sampling and noisy measurements introduce uncertainties and biases of the inferred orbital parameters. Uncertainties of the best-fitting models often cover qualitatively different configurations of studied systems. To mention just a few examples, we quote Kepler-223 (Mills et al. 2016), HD 202206 (Couetdic et al. 2010), ν-Octantis (Ramm et al. 2016; Goździewski et al. 2013), HR 8799 (Marois et al. 2010; Goździewski & Migaszewski 2014), HD 47366 (Sato et al. 2016). The dynamical analysis of the best-fitting planetary models has become a standard approach. For compact, resonant, strongly interacting systems, the optimization of observational models may benefit from implicit constraints of the dynamical stability (i.e., Goździewski et al. 2008; Goździewski & Migaszewski 2014).

Analysis of such problems relies on the so called fast dynamical indicators which are common for the dynamical systems theory. These numerical techniques make it possible to analyze effi-

⋆ e-mail: federico.panichi@stud.usz.edu.pl
† e-mail: krzysztof.gozdziewski@umk.pl
‡ e-mail: giorgio.turchetti@unibo.it
[1] http://exoplanetarchive.ipac.caltech.edu/

ciently large volumes of the phase/parameter-space. The fast indicators are developed to distinguish between stable and unstable (regular or chaotic) motions on the basis of relatively short arcs of phase-space trajectories of their dynamical systems. The most common tools in this class are algorithms based on the maximal Characteristic Lyapunov Exponent (mLCE, Benettin et al. 1980), the Fast Lyapunov Indicator (FLI, Froeschlé et al. 1997), the Mean Exponential Growth factor of Nearby Orbits (MEGNO, Cincotta & Simó 2000; Cincotta et al. 2003), the Smaller/Generalized Alignment Index (SALI and GALI, Skokos & Manos 2014), as well as on a few variants of refined Fourier frequency analysis, like the Numerical Analysis of Fundamental Frequencies (NAFF, Laskar 1990; Laskar et al. 1992), the Frequency Modified Fourier Transform (FMFT, Šidlichovský & Nesvorný 1996), the Spectral Number (SN, Michtchenko & Ferraz-Mello 2001).

In the realm of Hamiltonian formulation of the equations of motion, one may construct symplectic integrators (SI) which preserve the geometrical properties of the Hamiltonian flow (Hairer et al. 2002). Regarding the planetary N-body problem, SI are CPU efficient and reliable methods for long-term integration intervals and brought a breakthrough in this field (Wisdom & Holman 1991). Remarkably, SI are usually time-reversible (symmetric) schemes like the second order leapfrog (Yoshida 1990; Hairer et al. 2002).

A numerical breakup of the time-reversibility has been proved as sufficient condition to detect chaotic trajectories in the phase-space (Aarseth et al. 1994; Lehto et al. 2008; Faranda et al. 2012). Unlike regular orbits, an ergodic motion is expected to result in large displacements of the initial condition $\boldsymbol{x}_0$ after the forward and backward integration. Since SI are equivalent to symplectic maps, it makes it possible to determine and rigorously prove analytic properties of a numerical approach based on this idea developed in a series of papers (Turchetti et al. 2010a,b; Faranda et al. 2012; Panichi et al. 2016).

This relatively new dynamical fast indicator, called the Reversibility Error Method (REM) from hereafter, is based on the time reversibility of the ordinary differential equations (ODE). Rather then studying the dynamical structures with the *shadow particles* algorithm or with the variational equations (i.e., Benettin et al. 1980), it relies on integrating the same orbit forward and backward with a time-reversible (symmetric) numerical integrator. A phase space orbit may be classified w.r.t. the growth rate of the global error due to the accumulation of the round-off errors occurring in each integration step (forward and backward). If the orbit is regular, in the sense of mLCE, the accumulation of numerical errors develops as a power of time, $\sim t^{\alpha}$, while for mLCE-unstable trajectory its effect is exponentially amplified by its chaotic nature, $\sim \exp \lambda t$, where α and λ are real coefficients.

Numerical applications of REM to low-dimensional dynamical systems has revealed that it could be a sensitive and CPU efficient numerical fast indicator, indeed. Given its equivalent signature to mLCE (Turchetti et al. 2010a; Faranda et al. 2012), its advantage is a great simplicity of numerical implementation.

The main aim of this paper is to introduce the REM algorithm for studying dynamical properties of compact systems of Earth-like planets detected by the KEPLER mission. These systems are resonant or near-resonant, however with orbits in small and moderate eccentricity range. We intent to show that REM is as effective and precise fast indicator for this class of systems as common mLCE methods.

The paper is structured as follows. After Introduction, in Sect. 2, we briefly introduce the fast indicators REM, and MEGNO and FMFT as reference tools. Next, based on the perturbation criterion for near-integrable dynamical systems, we select a few examples to compare these indicators. Section 3 is devoted to a brief presentation of these dynamical systems. We recall a simple Hamiltonian system which exhibits the Arnold diffusion and the restricted three body problem. The main target of our work are compact 3−planet systems, HD 37124 and Kepler-60 with strong mutual perturbations, as well as 2−planet low-order MMR systems, Kepler-29, Kepler-26 and Kepler-36, which may be examples of "typical" near-resonant or resonant pairs of Super-Earth planets in the KEPLER sample. In Section 4 we present the results of numerical experiments with the fast indicators. Section 5 is devoted to numerical integrators, numerical accuracy and CPU efficiency of the REM. After Conclusions (Sect. 6), Appendix A shows a detailed theoretical background of this approach by comparing the Lyapunov error, due to the initial displacement, with the forward and reversibility errors due to random perturbations along the orbit.

2 DYNAMICAL FAST INDICATORS

A wide branch of the analysis of the long-term evolution of planetary systems relies on the numerical integration of the equations of motion (e.g., Wisdom & Holman 1991; Chambers 1999; Laskar & Robutel 2001; Ito & Tanikawa 2002; Laskar & Gastineau 2009). Besides the direct, long-term integrations of the equations of motion and analytic theories based on the averaging, the fast indicators are common tools to analyze the structure of chaotic and quasi-periodic motions in the phase-space. Here, we briefly describe REM and MEGNO, which may be considered as mLCE-related fast indicators, and a variant of the spectral algorithms, FMFT.

2.1 Reversibility Error Method (REM)

A formal derivation of REM for linear maps, its properties and the connection with mLCE are given in (Panichi et al. 2016). For Hamiltonian systems studied in this paper, which split for two individually integrable terms, we prove analytical properties of the reversibility error and a character of its changes for different regimes of motion. A detailed introduction and analysis of REM for nonlinear symplectic maps, which generalize the results in (Panichi et al. 2016), are given in Appendix A. Here we present only a brief and "practical" introduction.

Given an autonomous Hamiltonian system $\mathcal{H}$, the phase-space evolution of its solutions can be defined as the symplectic map $M(\boldsymbol{x})$ which iterates the conjugate variables $\boldsymbol{x}$,

$$\boldsymbol{x}_n = M(\boldsymbol{x}_{n-1}), \quad n = 1, \ldots, \tag{1}$$

n is the iteration index, and $\boldsymbol{x}_0$ is the initial condition, $\boldsymbol{x}_0 \equiv \boldsymbol{x}(t = t_0)$. We introduce a perturbed map $M_\gamma(\boldsymbol{x})$ where γ is a measure of the perturbation amplitude. For a generic Hamiltonian map, the reversibility error at iteration n is (see Appendix A),

$$d_n^{(\mathrm{R})} = \sqrt{\langle \left\| M_\gamma^{-n}(M_\gamma^n(\boldsymbol{x}_0)) - \boldsymbol{x}_0 \right\|^2 \rangle}, \tag{2}$$

where "$-n$" denotes the n-th backward iteration and "n" the n-th forward iteration of M_γ. The kind of perturbation and its amplitude are quite arbitrary: for Hamilton's flows it may the white noise, for a symplectic map it may be a random additive perturbation or the round-off error due to finite machine precision.

To apply Eq. 2 numerically, we must guarantee that the map is invertible (Faranda et al. 2012; Panichi et al. 2016). For a numerical integrator affected by a round-off error of amplitude γ, we change Eq. 2 into

$$d_n^{(R)} = \sqrt{\|\Phi^{\mathcal{H}}_{\gamma,-nh} \circ \Phi^{\mathcal{H}}_{\gamma,nh}(\boldsymbol{x}_0) - \boldsymbol{x}_0\|^2}, \tag{3}$$

where $\Phi^{\mathcal{H}}_{nh}$ denote a symplectic integrator scheme advancing the initial condition from $t = 0$ to $t = nh$, and h is the integration step. The scheme is time reversible, so that

$$\Phi^{\mathcal{H}}_{-h} \circ \Phi^{\mathcal{H}}_{h} \equiv id, \tag{4}$$

for one integration step h (Hairer et al. 2002). (Note that symplectic integrators may be not time-reversible integrators and vice-versa). The reversibility condition is lost for maps with the round-off and/local errors $\Phi^{\mathcal{H}}_{\gamma,nh}$. Note that in Eq. 3, we dropped the average which appears in Eq. 2, since unlikely for random perturbation, just a single realization of round-off errors is available.

The reversibility error is therefore the norm of the displacement from a selected initial condition in the phase-space, after integrating the equations of motion forward and back for the same time interval (number of steps).

Most symplectic integrator schemes $\Phi^{\mathcal{H}}_{h}$ used in practice are symmetric by design. If the Hamiltonian may be splitted for two terms, $\mathcal{H} = \mathcal{H}_A + \mathcal{H}_B$, which are individually integrable, then the second order leapfrog scheme

$$\Phi^{\mathcal{H}}_{h} \equiv \phi^{\mathcal{A}}_{h/2} \circ \phi^{\mathcal{B}}_{h} \circ \phi^{\mathcal{A}}_{h/2}, \tag{5}$$

is composed of symmetric flows $\phi^{\mathcal{A}}_t$ and $\phi^{\mathcal{B}}_t$ for Hamiltonians $\mathcal{H}_A$ and $\mathcal{H}_B$, respectively. This time-reversible concatenated scheme results in the local error $O(h^3)$.

A great advantage of the leapfrog is that it may be easily generalized to higher order schemes, as shown by Yoshida (1990). Here, we the 4th order integrator of Yoshida, as well as a family of symmetric integrators called SABA_n and SBAB_n (Laskar & Robutel 2001).

A typical behavior of REM for chaotic and regular phase-space trajectories is illustrated in Fig. 1. This shows time-evolution of REM computed for each individual planet in three-planet system HD 37124 (see Sect. 3.4.1 for details). The integration has been performed for the forward interval of 50 kyrs, and with the 4th order SABA_4 scheme with fixed time-step equal to 1 day. For each planet, REM increases following a power law w.r.t. integration time for a stable solution. We note that the deviation must increase due to the accumulation of the numerical round-off and, possibly, due to the local truncation error. We would like to note that the error with respect to exact flow depends on both the truncation error and the round-off and estimates are difficult unless one of them is dominant. For the chaotic orbit, the reversibility error increase rate has an exponential character. The crucial point is that the final REM deviations differ by ~ 7 orders of magnitude, and the orbits signatures could be easily distinguished each from other.

We make use of this property in Sect. 4 by constructing dynamical maps in planes of selected orbital and dynamical parameters. The REM outputs are classified through their character of time-variability and relative ranges. We note that a very similar calibration is known for FLI indicator (Froeschlé et al. 1997) or the mLCE itself, since these indicators do not offer an absolute measure of the instability degree in finite intervals of time.

2.2 Mean Exponential Growth factor of Close Orbits

Together with the evolution of the phase-space trajectory, Eq. 1, it is possible to propagate an initial displacement vector $\boldsymbol{\eta}$ with the

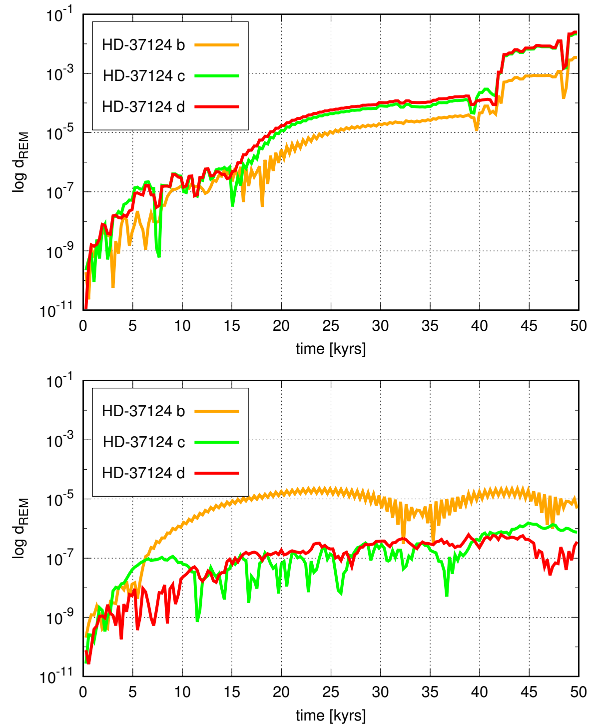

Figure 1. Time evolution of REM for the HD 37124 planetary system. The top panel is for unstable configuration, the bottom panel is for a stable, quasi-periodic solution. The REM is computed for each orbit separately, and marked with different colors (grey shades). The innermost planet (black) appears to be most influenced by the chaotic system, due to large value of REM (10^{-5}) at the end of the integration interval of 2×50 kyrs. The second planet (light-gray) and the third one (gray) exhibit slower increase of REM which reach 10^{-7} at the end of the simulation. For the unstable configuration, the REM components increase much faster, and they reach 0.1, a few orders of magnitude larger value than for the regular model.

tangent map DM defined as $DM_{ij} = \partial M_i / \partial \boldsymbol{x}_j$, $i, j = 1, \ldots 2N$, and N is the number of the degrees of freedom,

$$\boldsymbol{\eta}_n = DM(\boldsymbol{x}_{n-1})\boldsymbol{\eta}_{n-1}, \quad n > 0. \tag{6}$$

(See also Appendix A). This discretization is equivalent to solving the Hamiltonian ODE system including the equations of motion and the variational equations. The evolution of $\boldsymbol{\eta}(t)$ determines the maximal Characteristic Lyapunov Exponent (mLCE, Benettin et al. 1980)

$$\lambda \equiv \lim_{n\to\infty} \frac{1}{n} \log \frac{\|\boldsymbol{\eta}_n\|}{\|\boldsymbol{\eta}_0\|}, \quad \boldsymbol{\eta}_0 \equiv \boldsymbol{\eta}(t_0),$$

or its close relatives, like the Fast Lyapunov Indicator (FLI, Froeschlé et al. 1997) and the Mean Exponential Growth factor of Nearby Orbits (MEGNO, Cincotta & Simó 2000; Cincotta et al. 2003).

Though MEGNO has been primarily defined for continuous ODEs, here we choose its formulation for maps, consistent with REM formalism in other parts of this paper. It reads (Cincotta et al. 2003)

$$Y_n = \frac{2}{n} \sum_{k=1}^{n} k \ln \frac{\|\boldsymbol{\eta}_k\|}{\|\boldsymbol{\eta}_{k-1}\|}, \quad \langle Y \rangle_n = \frac{1}{n} \sum_{k=1}^{n} Y_k, \tag{7}$$

where $\boldsymbol{\eta}_k$ is the tangent vector at step k, $\boldsymbol{\eta}_0$ is random initial vector, $\|\boldsymbol{\eta}_0\| = 1$, and n is the number of steps. To propagate the MEGNO map Eqs. 7 for N-body planetary problem, we implemented (Goździewski et al. 2008) symplectic tangent map (Mikkola & Innanen 1999) that solves the equations of motion and the variational equations simultaneously.

The discrete map $\langle Y \rangle_n$ asymptotically tends to

$$\langle Y \rangle_n = an + b,$$

with $a = 0, b = 2$ for a quasi-periodic orbit, $a = b = 0$ for a stable, isochronous periodic orbit, and $a = \lambda/2$, $b = 0$ for a chaotic orbit, where λ is the mLCE approximation. Thus we can estimate the mLCE on a finite time interval by fitting the straight line to $\langle Y \rangle_n$ (see Cincotta et al. 2003, for details).

Since MEGNO is fully equivalent to FLI (Mestre et al. 2011), and makes it possible to estimate the mLCE values, we consider it as a well tested and representative fast indicator in the large family of variational algorithms (Barrio et al. 2009).

In general, the fixed step-size symplectic integrators cannot be used for configurations suffering from close encounters due to eccentric orbits. In such cases, we use the MEGNO formulation for ODEs (Cincotta & Simó 2000) with adaptive-step Bulirsh-Stoer-Gragg extrapolation method (Hairer et al. 2002, ODEX code).

2.3 Fourier Modified Frequency Transform

For one example, we used the Fourier Modified Frequency Transform (FMFT, Šidlichovský & Nesvorný 1996), which is classified as a spectral algorithm. We analyze the time series of heliocentric Keplerian elements $\mathcal{S}_i = \{a_i(t_k)\exp(\mathrm{i}\lambda_i(t_k)\}$ of planets $i = \mathrm{b}, \mathrm{c}, \mathrm{d}, \ldots$ and $k = 1, \ldots 2^N$, where N is the number of samples. These elements are inferred from canonical Poincaré coordinates through usual two-body orbit transformation (Morbidelli 2002). For a near-integrable planetary system, the FMFT transform of such series provides one of the fundamental, canonical frequencies, namely the proper mean motion, n_i associated with the largest amplitude a_i^0 of signal $\mathcal{S}_i$.

We are interested in the diffusion of these proper mean motions, hence for each planet we define a coefficient of the diffusion of fundamental frequencies (Robutel & Laskar 2001):

$$\sigma_f = \frac{n_{\Delta t \in [0,T]}}{n_{\Delta t \in [T,2T]}} - 1, \quad T = Nh\,,$$

where h is the sampling step. If the frequencies for time intervals $\Delta t \in [0,T]$ and $\Delta t \in [T,2T]$ do not change, the motion is quasi-periodic, while σ_f different from zero indicates a chaotic solution. This fast indicator has been proved to be very sensitive for chaotic motions (Robutel & Laskar 2001; Šidlichovský & Nesvorný 1996).

3 BETWEEN STRONG AND WEAK PERTURBATIONS

We consider a near-integrable Hamiltonian system

$$\mathcal{H}(\boldsymbol{I}, \boldsymbol{\theta}) = \mathcal{H}_0(\boldsymbol{I}) + \varepsilon \mathcal{H}_1(\boldsymbol{I}, \boldsymbol{\theta}), \quad \varepsilon \in [0,1), \tag{8}$$

composed of integrable term $\mathcal{H}_0(\boldsymbol{I})$ and perturbation $\varepsilon\mathcal{H}_1(\boldsymbol{I}, \boldsymbol{\theta})$, w.r.t. the action–angle variables $(\boldsymbol{I}, \boldsymbol{\theta})$. We assume that $\|\mathcal{H}\|_0 \simeq \|\mathcal{H}\|_1$. A feature determining the phase-space structure of this system are resonances between the fundamental frequencies, $\dot{\boldsymbol{\omega}}_0 = \partial\mathcal{H}_0(\boldsymbol{I})/\partial\boldsymbol{I}$. They govern the long-term evolution of the phase-space trajectories. Depending on the perturbation strength, the chaotic diffusion along these resonances (Morbidelli & Giorgilli 1995; Guzzo et al. 2002) may lead to macroscopic, geometric changes of the phase-space trajectories. A simple measure of the complexity of a dynamical system and chaotic diffusion is the perturbation parameter ε, which may be expressed by the norm ratio of the perturbed $\|\mathcal{H}_1\|$ to the integrable $\|\mathcal{H}_0\|$ term. The KAM theorem (Kolmogorov 1954; Moser 1958; Arnold 1963) guarantees the existence of KAM invariant tori until when the value of the perturbation is smaller than some threshold depending on particular resonance. After that threshold, the KAM tori are destroyed and the absence of topological barriers allow the chaotic trajectories to globally diffuse (Chirikov 1979; Froeschlé et al. 2005).

In this paper, we consider a few models of the form Eq. 8 and different perturbation strength. We focus on numerically detecting their resonant structures with the help of fast indicators.

To solve the equations of motion and the variational equations associated with model Eq. 8, required to determine MEGNO, we use a family of symplectic, symmetric integrators SABA$_n$/SBAB$_n$ (Laskar & Robutel 2001) which exhibit the local error $O(\varepsilon^2 h^2 + \varepsilon^2 h^n)$, where n is the order of the scheme, and h is time step-size. Therefore, for splittings that provides ε small, as in Eq.8, these schemes usually behave as higher order integrators without introducing negative sub-steps (Laskar & Robutel 2001). Therefore even the second-order, modified SABA$_2$/SBAB$_2$ schemes as well as the second order leapfrog with local error $O(\varepsilon h^3)$ offer sufficient accuracy and small CPU overhead. (More technical details are presented in Sect. 5).

3.1 A Hamiltonian with the Arnold web presence

The first example for the REM and MEGNO tests is a 3-dim Hamiltonian system introduced by (Froeschlé et al. 2000) to study qualitative features of the resonance overlap in the phase-space of conservative Hamiltonian systems. The Froeschlé–Guzzo–Lega (FGL from hereafter) Hamiltonian reads

$$\mathcal{H}(\boldsymbol{I}, \boldsymbol{\theta}) = \frac{I_1^2 + I_2^2}{2} + I_3 + \frac{\varepsilon}{\cos(\theta_1) + \cos(\theta_2) + \cos(\theta_3) + 4}. \tag{9}$$

Perturbation term $\mathcal{H}_1(\boldsymbol{\theta})$ scaled by $\varepsilon \in [0,1)$ depends only on angles $\theta = [\theta_1, \theta_2, \theta_3]$. The fundamental frequencies exhibit full Fourier spectrum. Resonances description may be reduced to a relation between actions $\boldsymbol{I} = [I_1, I_2, I_3]$ through $m_1 I_1 + m_2 I_2 + 2\pi m_3 = 0$, with $m_1, m_2, m_3 \in \mathbb{Z}/0$ (see Froeschlé et al. 2000, for details). They form a dense net, and their widths depend on ε. Overlapping of these resonances leads to fractal structures in the phase-space, interpreted as the Arnold web. Due to complexity of these dynamical structures and rich long-term dynamical behaviors, which are provided by a very simple equations of motion, Hamiltonian Eq.9 is a great model to test numerical integrators and fast indicators. This three-degrees of freedom dynamical system exhibits all qualitative features which may be found in multi-dimensional N-body systems.

3.2 The circular restricted three body problem

Perhaps the most attractive passage between simple dynamical systems and planetary systems is the circular restricted three body problem (RTBP). We use this model to demonstrate the REM algorithm and equivalence of the results when the equations of motion are solved by relatively simple symplectic algorithms.

The RTBP may be considered as the limit case of the N-body planetary problem, when the star and a massive planet are primaries moving in a circular, Keplerian orbit, and we investigate the motion of a mass-less particle (i.e.: an asteroid, a comet). Any "regular"

2−planet system may be transformed to the RTPB by setting the mass of one planet to zero, and fixing a circular orbit of the second one. Then we may solve the equations of motion with an appropriate algorithm.

The same problem may be described in the non-inertial frame rotating with the apsidal line of the primaries. Its dynamics is governed by the Hamiltonian

$$\mathcal{H}(p_x,p_y,x,y) = \mathcal{T}(p_x,p_y,x,y) + \mathcal{U}(x,y) \equiv \mathcal{H}_A + \mathcal{H}_B, \qquad (10)$$

where the kinetic energy $\mathcal{T} p_x,p_y,x,y) \equiv \mathcal{H}_A(p_x,p_y,x,y)$ reads

$$\mathcal{T}(p_x,p_y,x,y) = \frac{1}{2}\left(x-p_y\right)^2 + \frac{1}{2}\left(y+p_x\right)^2, \qquad (11)$$

and the potential energy $\mathcal{U}(x,y) \equiv \mathcal{H}_B(x,y)$ is

$$\mathcal{U}(x,y) = -\frac{x^2+y^2}{2} - \frac{1-\mu}{\rho_1} - \frac{\mu}{\rho_2}, \qquad (12)$$

where (x,y) are barycentric coordinates and momenta (p_x,p_y) of the massless particle, and its distances from primaries

$$\rho_1^2(x,y) = (x+\mu)^2 + y^2, \quad \rho_2^2(x,y) = (x+1-\mu)^2 + y^2.$$

Each term of Eq. 10 in the absence of the other generates the equations of motion are soluble.

The equations of motion of the kinetic part expressed by the gradient components of $\mathcal{T}$ w.r.t. (p_x,p_y,x,y) canonical coordinates,

$$\dot{x} = \mathcal{T}_{p_x}, \quad \dot{y} = \mathcal{T}_{p_y}, \quad \dot{p}_x = -\mathcal{T}_x, \quad \dot{p}_y = -\mathcal{T}_{p_y}, \qquad (13)$$

form the linear ODE system, which has a well known solution (e.g., Dulin & Worhington 2014) equivalent to $\phi_h^{\mathcal{A}}$,

$$\begin{aligned} x(h) &= b_1\sin(2h) + b_2\cos(2h) + c_1, \\ y(h) &= b_1\cos(2h) - b_2\sin(2h) + c_2, \\ p_x(h) &= b_1\cos(2h) - b_2\sin(2h) - c_2, \\ p_y(h) &= -b_1\sin(2h) - b_2\cos(2h) + c_1, \end{aligned} \qquad (14)$$

where coefficients b_1,b_2,c_1,c_2 are expressed through the initial condition $(p_{x,0},p_{y,0},x_0,y_0)$, i.e., the momenta and coordinates at time $t_0 = 0$,

$$\begin{aligned} b_1 &= \tfrac{1}{2}\left(y_0 + p_{x,0}\right), \quad b_2 = \tfrac{1}{2}\left(x_0 - p_{y,0}\right), \\ c_1 &= \tfrac{1}{2}\left(x_0 - p_{y,0}\right), \quad c_2 = \tfrac{1}{2}\left(y_0 - p_{x,0}\right). \end{aligned} \qquad (15)$$

The equations of motion for the potential are even more simple,

$$\dot{x} = 0, \quad \dot{y} = 0, \quad \dot{p}_x = -\mathcal{U}_x, \quad \dot{p}_y = -\mathcal{U}_y, \qquad (16)$$

where $\mathcal{U}_x$ and $\mathcal{U}_y$ are gradient components of the potential $\mathcal{U}$. The solution to these equations, equivalent to $\phi_h^{\mathcal{B}}$, is essentially trivial,

$$\begin{aligned} x(h) &= x_0, \\ y(h) &= y_0, \\ p_x(h) &= -\mathcal{U}_x(x_0,y_0)h + p_{x,0}, \\ p_y(h) &= -\mathcal{U}_y(x_0,y_0)h + p_{y,0}. \end{aligned} \qquad (17)$$

Splitting for Hamiltonians $\mathcal{T}$ and $\mathcal{U}$ is non-natural in the sense that the kinetic energy in non-inertial, rotating frame depends not only on momenta, but also on coordinates.

3.3 *N*–body planetary problem

We define the main target of our numerical experiments, which is the *N*-body planetary problem, w.r.t. canonical heliocentric Poincaré coordinates (Morbidelli 2002), sometimes called the democratic heliocentric-barycentric coordinates. We apply the same formulation as in (Goździewski et al. 2008). The Hamiltonian is composed of two terms $\mathcal{H} = \mathcal{H}_0 + \mathcal{H}_1$. The first term reads

$$\mathcal{H}_0(\boldsymbol{p},\boldsymbol{r}) = \frac{1}{2}\sum_{i=1}^{N}\frac{\boldsymbol{p}_i^2}{m_i} - k^2 m_0 \sum_{i=1}^{N}\frac{m_i}{r_i}, \qquad (18)$$

where k^2 is the Gauss gravitational constant, $\boldsymbol{p}_i = m_i \boldsymbol{v}_i$ are the canonical (barycentric) momenta, m_i the mass of the $i-th$ planet, $\boldsymbol{v}_i$ is for its barycentric velocity and $\boldsymbol{r}_i$ the heliocentric coordinates of the planet, and m_0 is the stellar mass.

The second term of the Hamiltonian, which is the perturbation of Keplerian orbits due to the mutual interactions of the planets in the system, is defined as

$$\mathcal{R} \equiv \varepsilon\mathcal{H}_1(\boldsymbol{p},\boldsymbol{r}) = \frac{1}{2\,m_0}\left(\sum_{i=1}^{N}\boldsymbol{p}_i\right)^2 - k^2\sum_{i=1}^{N}\sum_{j=i+1}^{N}\frac{m_i\,m_j}{\|\boldsymbol{r}_i - \boldsymbol{r}_j\|}. \qquad (19)$$

Hamiltonian $\mathcal{H}$ is equivalent to the direct sum of N integrable Keplerian Hamiltonians perturbed by the mutual gravitational potential of the planets. Since $\mathcal{H}_1$ does not depend on velocities (momenta), both terms are integrable in the absence of each other. This leads to natural splitting used to construct the symplectic planetary integrators prototyped in the remarkable paper of Wisdom & Holman (1991). Their scheme is based on splitting the planetary Hamiltonian in Jacobi-coordinates, and may be generalized for other splittings, like that one we applied here.

Table 1. Nominal, osculating heliocentric Keplerian elements for planetary systems tested in this paper. The masses of parent stars are $0.78\,\mathrm{m}_\odot$ for HD 37124 (Vogt et al. 2005), $0.55\,\mathrm{m}_\odot$ for Kepler-26, $1.105\,\mathrm{m}_\odot$ for Kepler-60 and $1.071\,\mathrm{m}_\odot$ for Kepler-36, $1.0\,\mathrm{m}_\odot$ for Kepler-29 (Rowe et al. 2015). All systems are coplanar with $I = 90^\circ$ and $\Omega = 0^\circ$.

System	$m\,[\mathrm{m}_\oplus]$	$a\,$[au]	e	$\varpi\,$[deg]	$\mathcal{M}\,$[deg]
HD 37124 b	198	0.51866	0.079	138.4	259.0
HD 37124 d	180	1.61117	0.152	268.9	109.5
HD 37124 d	226	3.14451	0.297	269.5	124.1
Kepler-26 b	5.1	0.08534	0.042	9.6	190.3
Kepler-26 c	6.3	0.10709	0.025	−18.6	257.2
Kepler-29 b	7.7	0.09192	0.006	23.6	313.9
Kepler-29 c	6.3	0.10872	0.007	−151.8	29.0
Kepler-60 b	4.6	0.07497	0.115	−145.4	−158.4
Kepler-60 c	4.9	0.08700	0.069	−128.5	−292.6
Kepler-60 d	4.8	0.10558	0.088	−152.1	−345.1
Kepler-36 b	4.2	0.11541	0.044	−126.5	212.4
Kepler-36 c	7.6	0.12840	0.020	−158.7	24.0

3.4 A characterization of tested planetary systems

Table 1 displays orbital elements and masses of five resonant planetary systems tested in the next Section. Table 2 displays estimates of the perturbation parameter ε, which may be the measure of complexity of systems in Tab. 1. The strength of mutual perturbations affects and forces non-Keplerian evolution of the orbits, which we expect to be revealed in dynamical maps obtained with the fast indicators.

We determine this parameter for the nominal initial conditions as $\varepsilon(t=0)$, see Tab. 2. Obviously, ε is a function of time, and, as illustrated for HD 37124 system (Fig. 2), it may vary during the

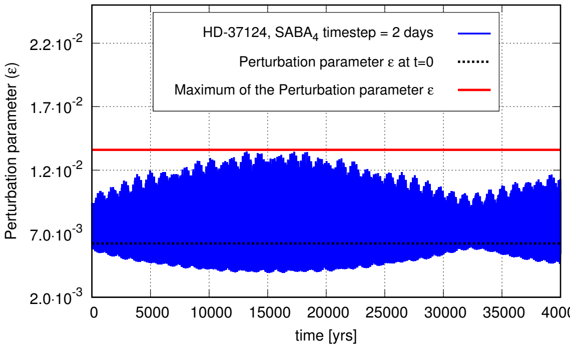

Figure 2. Variability of the perturbation parameter $\varepsilon(t)$ for HD 37124 initial condition (Tab. 1). The initial condition has been integrated for 40 kyrs.

Table 2. Planetary systems classified by the perturbation parameter $\varepsilon \equiv \|\mathcal{R}/\mathcal{H}_0\|$. Units are scaled with the choice of the Gaussian constant $k^2 = 1$. We consider coplanar systems, hence the number of the degrees of freedom for each system is $4 \times N$, where N is the number of planets.

system	$\|\mathcal{H}_0\|$	$\|\mathcal{R}\|$	$\varepsilon(t=0)$	$\varepsilon \equiv \max\varepsilon$
HD 37124 b,c,d	6×10^{-11}	4×10^{-13}	6×10^{-3}	1.3×10^{-2}
Kepler-26 b,c	9×10^{-12}	2×10^{-15}	2×10^{-4}	2.5×10^{-4}
Kepler-60 b,c	2×10^{-11}	3×10^{-15}	1×10^{-4}	1.6×10^{-4}
Kepler-36 b,c	1×10^{-11}	2×10^{-15}	2×10^{-4}	1.3×10^{-4}
Kepler-29 b,c	5×10^{-12}	3×10^{-16}	5×10^{-5}	5.3×10^{-5}

orbital evolution. Therefore, we integrated all systems in Tab. 1 for 2×10^3 outermost orbits, and we choose the maximal ε attained during the integration as the measure of the perturbation. We also note, that $\max\varepsilon$ in Tab. 2 is only a reference value for dynamical maps, which span a range of orbital elements around the nominal parameters.

We briefly characterize the sample of planetary systems below.

3.4.1 *HD 37124: three planets in Jovian mass range*

The HD 37124 planetary system (Vogt et al. 2005) is likely a compact configuration of three massive, Jovian-like planets discovered with the Radial Velocity technique. Its dynamics has been intensively investigated (Goździewski et al. 2008; Baluev 2008; Wright et al. 2011). The perturbation parameter ε depends not only on the number of planets, but also on their mutual distance and their masses. Since we intent to use reversible symplectic integrators with constant step-size, even moderate eccentricities of compact orbits may be challenging for such numerical schemes, in the sense of accuracy and conservation of the integrals of motion. HD 37124 planetary system may be a good example of such demanding system. Its Jovian companions are present in a region spanned by low-order 2-body and 3-body MMRS (Goździewski et al. 2008; Baluev 2008). Given their relatively large masses, the expected mutual gravitational interactions between the planets are the strongest in the sample, as shown in Tab. 2.

3.4.2 *Kepler-26: two planets near 7:5 MMR*

A resonant planetary system that exhibits complex dynamics is Kepler-26 (Steffen et al. 2012). It consist of two super-Earth planets near to the second order 7:5 MMR. Since the orbits may appear very near one to another, the mutual gravitational interaction may become also very strong. Kepler-26 has the largest ε value among KEPLER systems displayed in Table 2. We note that actually Kepler-26 hosts four confirmed planets (Jontof-Hutter et al. 2016) but we neglect the innermost and the outermost planet since the available observations do not make it possible to reliably constrain their orbits and physical properties. The two-planet configuration is selected merely to have an example of a particular resonant system. This is motivated through the recent studies of this system (Jontof-Hutter et al. 2016; Hadden & Lithwick 2015; Deck & Agol 2016). We determined the planetary masses through re-analysis of the long cadence Q1-Q17 TTV dataset in (Rowe et al. 2015).

3.4.3 *Kepler-60: three super-Earths in the Laplace resonance*

Recently, Goździewski et al. (2016) analyzed the Kepler-60 extrasolar system and two resonant best-fitting solutions to the long cadence TTV measurements were found. Both of them may be interpreted as generalized, zeroth-order three-body mean motion Laplace resonance. The Kepler-60 is an example of an extremely compact configuration of relatively massive planets in orbits with periods of $\simeq 7.1$, $\simeq 8.9$ and $\simeq 11.9$ days, respectively. This resonance could be either a “pure” three-body MMR with only the Laplace critical argument $\phi_L = \lambda_b - 2\lambda_c + \lambda_d$ librating with a small amplitude, or it may simultaneously form a chain of two-body $5:4$ and $4:3$ MMRs. In both cases the resonant Kepler-60 system is dynamically active and exhibits complex dynamics, both regarding limited zones of stable motions in the phase-space, as well as the presence of Arnold web structures. Given the close orbits, it is also a very demanding orbital configuration for tracking the long-term evolution and stability.

3.4.4 *Kepler-36: massive super-Earths in stable chaos?*

The Kepler-36 system is one of the first configurations detected with the analysis of its clear TTV signal (Deck et al. 2012). It exhibits the smallest ε in the sample shown in Tab. 2. This system brought our attention due to the presence of the so called *stable chaos* (Deck et al. 2012). To verify this phenomenon with more recent TTV data, we did a preliminary re-analysis of the Q1-Q17 TTV measurements with the genetic algorithm (Charbonneau 1995). We choose one of the best-fitting orbital solutions displayed in Tab. 1 for numerical tests of REM.

3.4.5 *Kepler-29: two super-Earths in 9:7 MMR*

We re-analyze the TTV measurements of the Kepler-29 system discovered in (Fabrycky et al. 2012) in our forthcoming paper. This extremely compact configuration of two massive super-Earth planets in ~ 5 Earth mass range is separated at conjunctions by only $\simeq 0.01$ au. The planets are likely involved in an exact 9:7 MMR.

For the REM analysis we used osculating elements in Tab. 1. The first N-body model accounts for the mutual interactions of the planets. Given so close orbits, the Kepler-29 configuration is also an interesting model for the REM test in the framework of RTBP with two different splitting schemes of the Hamiltonian. We transformed the observational system to the RTBP model by fixing the inner mass to zero and the orbital eccentricity of the outer planet also to zero. (In fact, this eccentricity may be very small, $e_c \simeq 0.001$ in the real system). This example is used as a transition model between a simple, low-dimensional dynamical system and the full N-body formulation.

4 RESULTS AND INTERPRETATION

In this Section we describe the results of testing chaotic indicators defined in Sect. 2, when applied to systems defined in Sect. 3, and characterized in Table 2.

Those configurations are non-integrable multi-dimensional conservative systems exhibiting resonant structures. We aim to detect these structures using 2-dim dynamical maps (grids) composed of two model parameters selected in a given initial condition. Usually, we choose the semi-major axis – eccentricity, (a, e)-plane for a selected planet, since these elements are rescaled canonical actions of the planetary Hamiltonian, Eq. 8. We vary these parameters along axes of the grid within certain ranges, and the dynamical signatures of phase trajectories are then computed in each point of the grid. The results are color-coded and marked in 2-dim maps.

We are interested in a reliable detection of resonance structures, therefore time scales as many as 10^5–10^6 characteristic periods (outermost orbits) must be analyzed. We also compute high-resolution scans, up to 1024×1024 points, to avoid missing fine structures of the phase-space. Such resolutions chosen for our numerical experiments may be redundant for routine computations, yet they may cause a huge, non-realistic CPU overheads, depending on particular algorithms.

For all numerical experiments, we used our multi-CPU, "embarrassingly parallel" farm code μFARM (Goździewski, in preparation) armed with a number of different fast indicators, which makes use of the Message Passing Interface (MPI) and GCC ver. 4.8. Intensive computations have been performed on Intel Xeon CPU (E5-2697, 2.60GHz) of the EAGLE cluster at the Poznań Supercomputing and Networking Center. We refer to this particular CPU quoting code execution timings, and they should be used comparatively.

Finally, we do not intent to analyze the dynamical systems in detail. We focus on the sensitivity of the fast indicators for fine structures in the phase-space, associated with complex borders of chaotic and regular motions, the presence of separatrices and secondary resonances.

4.1 System 1: FGL Hamiltonian system

A Hamiltonian defined by Eq. 9 and the corresponding symplectic map version were studied for resonances and chaotic diffusion phenomena (Froeschlé et al. 2000, 2005), with the help of fast indicators FLI and MEGNO (Słonina et al. 2015). The REM algorithm has been already tested for this Hamiltonian system by Faranda et al. (2012) with the canonical map technique for relatively small 10^3 iterations. Here, we extend the integration time to 10^6–10^7 characteristic periods. To preserve a homogeneous computing environment, we computed the REM map with the symplectic $SABA_3$ scheme. For MEGNO, we used the symplectic tangent map (Mikkola & Innanen 1999), in accord with Eq. 7. Also $SABA_3$ scheme has been used.

The results of integrations for 10^6 time units are illustrated in Fig. 3. Dynamical maps are shown in the (I_1, I_2)-plane, and show a small portion of the Arnold web for $\varepsilon = 0.01$. It is significantly smaller from $\varepsilon = 0.04$ which was found as the borderline value for the global overlap of resonances, i.e., between Nekhoroshev and Chirikov regimes of the dynamics in this system (Froeschlé et al. 2000).

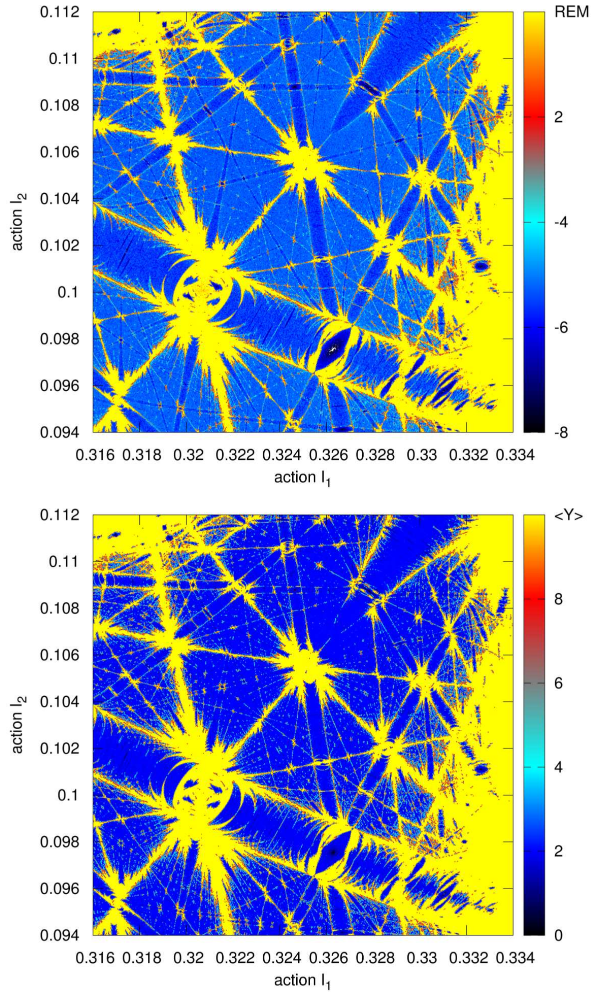

Figure 3. A comparison of REM (*top panel*, note the logarithmic scale) and MEGNO (*bottom panel*, symplectic tangent map algorithm) for the FLG Hamiltonian. The map is computed in a 1024×1024 grid of initial conditions in the (I_1, I_2)-plane of actions. Perturbation parameter $\varepsilon = 0.01$. The integrations were performed with the third-order $SABA_3$-scheme, time-step of $h = 0.29$ and for 10^6 time units. Integrations of MEGNO were interrupted if $\langle Y \rangle > 10$. This time-step provides the relative energy conservation to $\sim 10^{-10}$. The CPU overhead for single initial condition is ~ 1 second for REM, and between 0.1 and ~ 3 seconds for MEGNO.

Periodic (black), resonant (blue/dark blue or gray) and chaotic (yellow/red or light gray) orbits are present in both maps which are in a close correspondence. Inspecting them, we may notice subtle resonant structures between sharp (yellow/light gray) separatrices which are differentiated better from neighbouring trajectories in the REM map. We note that some very weak structures could be missing in the MEGNO map due to non-optimal choice of the initial variations $\boldsymbol{\eta}$ that are required to solve the deviation $\delta(t) \equiv \|\boldsymbol{\eta}\|$. To avoid systematic effects, we usually choose it randomly, following Cincotta et al. (2003). However, better strategies could be applied (Barrio et al. 2009), for instance, by selecting the initial $\boldsymbol{\eta}$ as the unit vector parallel to $\nabla\mathcal{H}$.

In the next Fig. 4 a larger portion of the phase-space is illustrated for 10^7 time units. In this experiment, REM attains values of 10^3 for chaotic orbits, and 10^{-4}, for regular orbits. Nevertheless,

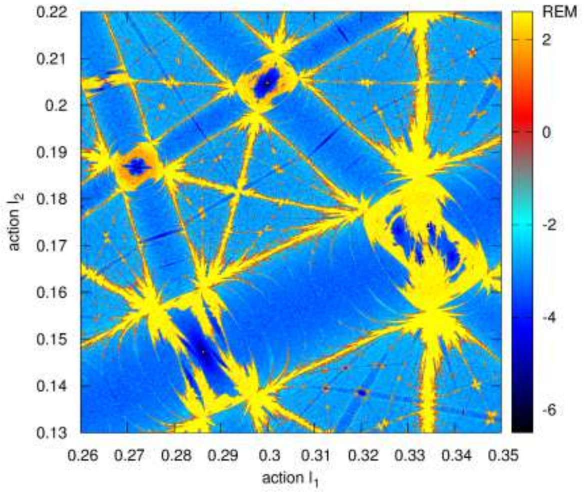

Figure 4. The REM dynamical map for the FLG Hamiltonian. The map is computed in a 1024×1024 grid of initial conditions in the (I_1, I_2)-plane of actions. Perturbation parameter $\varepsilon = 0.007$. The integrations were performed with the third-order SABA$_3$-scheme, time-step of $h = 0.29$ and for 10^7 time units.

only the overall variability range is essential to detect all fine structures of the phase-space. The stable periodic orbits are detected at the centers of overlapping resonances, as well resonances' widths are marked as darker blue/gray shades limited by yellow and orange (light gray) separatrices. The CPU overhead per one initial conditions is very different for both algorithms. For regular trajectories it is two times smaller for REM than for MEGNO. For chaotic and strongly chaotic trajectories, the MEGNO CPU overhead may be as small as $\sim 10\%$ of constant CPU overhead for REM, given the chaotic signature of chaotic orbits may be examined "on-line", by tracking whether the current value of $\langle Y \rangle < \langle Y \rangle_{\rm lim}$, where $\langle Y \rangle_{\rm lim} \gg 2$. The total integration time is similar, however the REM implementation could be considered next to trivial.

4.2 System 2: HD 37124, three sub-Jupiter system

Here we use the initial condition for HD 37124 system in (Goździewski et al. 2008), which leads to dynamical structures in the semi-major axes plane closely resembling the Arnold web in the model Hamiltonian, Eq. 9.

Figure 5 shows such a map in the $(a_{\rm c}, a_{\rm d})$-plane. The grid resolution is 640×640 initial conditions, the integration time is 50 kyrs. The REM has been integrated with the SABA$_3$-scheme with the time-step of 5 days, while the Bulirsch-Stoer-Gragg ODEX integrator relative and absolute accuracy has been set to 10^{-14}. In this example, we used this general purpose ODE solver for a reference, to obtain a reliable dynamical map. Strong gravitational interaction between massive planets are expected, and the tested configuration resides in collisional, very chaotic zone.

Both dynamical maps agree very well, and all dynamical features may be found. We note however, that this is rather a borderline case of REM application, due to strongly chaotic regime. Also, due to fast linear growth of MEGNO for chaotic orbits in this zone, unstable motions are quickly detected. Hence the integration time may be greatly reduced when some prescribed limit is reached. This is not the case for REM, because, usually, the whole integration must

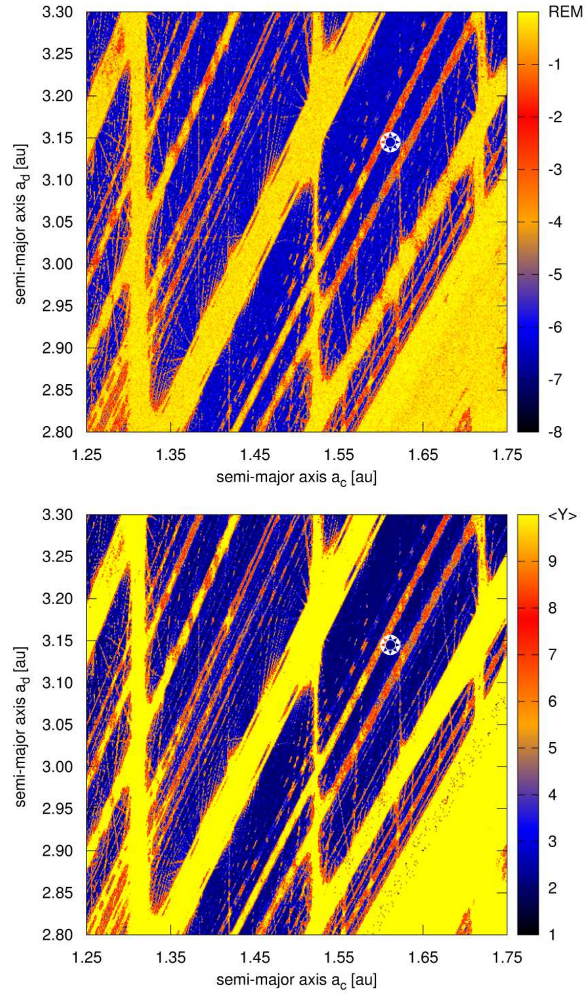

Figure 5. REM and MEGNO maps for the HD 37124 system presented in $(a_{\rm c}, a_{\rm d})$-plane. SABA$_3$ REM algorithm with time-step of 5 days and forward integration time of 50 kyrs took ~ 30 seconds per initial condition. The CPU overhead for MEGNO was varied between ~ 1 to ~ 22 seconds, given limiting $\langle Y \rangle = 10$. The star symbol marks the nominal initial condition displayed in Tab. 1.

be performed before it value could be determined. However, the algorithm provides reliable results even in such a difficult case.

4.3 System 3: Kepler-26 planetary system near 7:5 MMR

The orbital period ratios of the inner pair of super-Earth in the Kepler-26 system are close to the second order 7:5 MMR. Dynamical maps in the $(a_{\rm b}, e_{\rm b})$-plane shown in Fig. 6 illustrate a complex shape of the resonance. Both REM and MEGNO unveil its peculiar separatrix structure in its interior part, which exhibits a few disconnected stable regions.

In this experiment, we applied the most CPU efficient implementation of REM, which we classify as the second order leapfrog-UVC(5) algorithm in accord with Sec. 5. It is the mixed-variable scheme with Keplerian drift in universal variables without Stumpff series Wisdom & Hernandez (2015) and symplectic correctors (Wisdom 2006) of the 5th order. For computing the MEGNO map, we used the tangent map algorithm and SABA_4 scheme. The forward integration time of 16 kyrs is the same for both algorithms (we note that REM requires effectively 32 kyrs integration), which is equivalent to 5×10^5 outermost orbits.

The overall structure of the 7:5 MMR and higher order MMRs are the same in both maps. The algorithms reveal subtle stepping structure of chaotic configurations (around 0.855 au and eccentricity around 0.12) as well as tiny islands of stable motion at the top of both maps. However, the elliptic shape of strong chaos surrounding weaker chaotic motions present in the MEGNO map are missing in the REM map. We attribute such structures to the presence of secondary resonances (Morbidelli 2002) within the MMR zones.

The REM map involve a signature of the collision zone of orbits defined geometrically as the solution to $a_\mathrm{b}(1+a_\mathrm{b})=a_\mathrm{c}(1-a_\mathrm{c})$. *A dynamical border* of this zone may be seen as a change of shades across the REM map, around $e_\mathrm{b}\simeq 0.14$. This zone appears below a collision curve determined by the semi-major axis $(a_\mathrm{c}-R_H)$, where R_H is the mutual Hill radius for circular orbits

$$R_H=\sqrt[3]{\frac{m_\mathrm{b}+m_\mathrm{c}}{3M_\star}}\,\frac{a_\mathrm{b}+a_\mathrm{c}}{2},$$

and $m_\mathrm{b,c}$, $a_\mathrm{b,c}$ are the masses and semi-major axes of the planets, $M_\star$ is the stellar mass. This curve is marked with thin, grey curve in the REM map. This feature illustrates that the leapfrog-UVC(8) algorithm is robust for such near-collisional configurations, in spite that the step-size was kept constant across the whole grid.

We conclude that this experiment brings a warning that in particular cases, when we are interested in a comprehensive detection of fine structures of the MMRs, the results of different fast indicators should be compared, and we should not rely on one, particular indicator. Nevertheless, in this example the REM detected major MMR's structures and the shape of chaotic zone for relatively small CPU overhead. A single REM integration took 30 s, while the symplectic SABA_4 MEGNO algorithm with the same step size and upper limit of $\langle Y\rangle=256$ has required up to 100 s. The key factor that reduced the CPU overhead is the leapfrog scheme.

4.4 System 4: the Laplace resonance in Kepler-60

The Kepler-60 system has been comprehensively analyzed in (Goździewski et al. 2016), also regarding its dynamical structure. In Figure 7 we illustrate non-published MEGNO map (bottom panel) in the $(\varpi_\mathrm{c},\varpi_\mathrm{d})$-plane that reveals a complex structure of the Laplace resonance around one of the best-fitting solutions (marked with a star symbol) to the TTV measurements in (Rowe et al. 2015), Table 1. The top panel shows a high resolution REM map derived with the leapfrog-UVC(5) integrator for 18 kyrs, with the time-step of 0.125 d. With this time-step, the CPU overhead is huge, ~ 80 s per stable initial condition, i.e., still about two times smaller than the mean CPU time for MEGNO with the SABA_4 and the same time-step and forward integration interval. This CPU time may be reduced with larger time-steps, since our choice is rather very conservative. We note however that a significant fraction of the grid is spanned by strongly chaotic configurations, which are detected by MEGNO within a few seconds.

4.5 System 5: Kepler-36 planetary system in 7:6 MMR

Dynamical maps in the $(a_\mathrm{b},e_\mathrm{b})$-plane for Kepler-36 (Deck et al. 2012), near to the first order 7:6 MMR are presented in Fig. 8. Both maps have been integrated for 36 kyrs. MEGNO is computed with the 4th order SABA_4 scheme and the tangent map algorithm

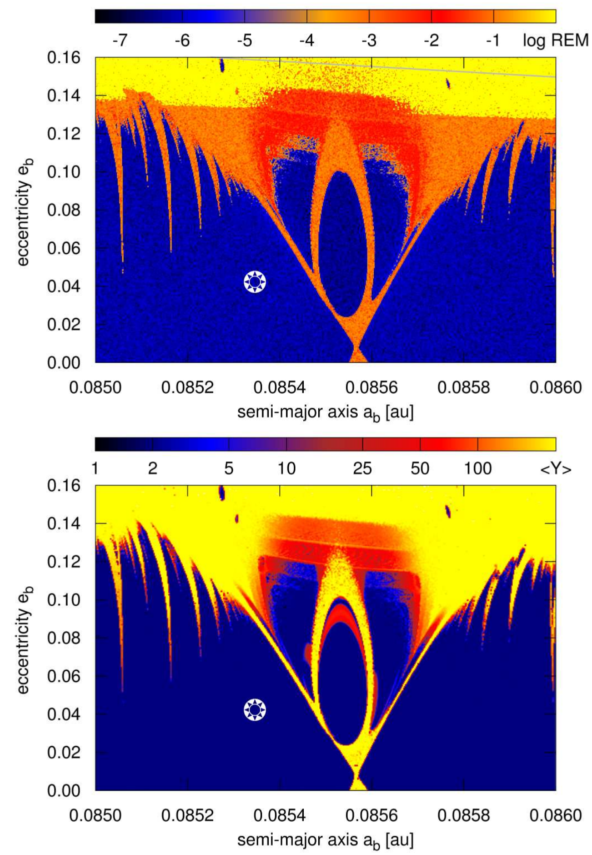

Figure 6. MEGNO and REM comparison for Kepler-26. *Top panel*: the REM map in $(a_\mathrm{b},e_\mathrm{b})$-plane computed for a grid of 640×480 points, the second order lapfrog-UVC(5) with time-step 0.25 days, and the forward integration interval 18 kyrs. *Bottom panel* is for symplectic MEGNO map in the $(a_\mathrm{b},e_\mathrm{b})$-plane computed with SABA_4 scheme and time-step 0.5 days integrated for 16 kyrs in a grid of 512×384 points and with a maximum value of $\langle Y\rangle$ equal to 256. Thin white curve in the upper-right corner marks the collision of orbits, and thick gray curve marks the mutual Hill radius separation of the orbits. The perturbation parameter $\max\varepsilon$ vary across the map between $\sim 2.4\times10^3$ and $\sim 3\times10^{-3}$, see also Tab. 2. The star symbol marks the nominal initial condition displayed in Tab. 1.

(Goździewski et al. 2008) with the time-step 0.25 days. REM is computed with the leapfrog-UVC(5) for the same forward integration interval (effectively it is two times longer for REM). We selected time-step of 0.25 days and that conserved the energy to 10^{-9} in relative scale. CPU overhead per initial condition was ~ 37 s, and between 3 and 130 seconds for MEGNO. In the later case, the CPU overhead depends on the local value of mLCE, since we have set-up rather large limit of $\langle Y\rangle_\mathrm{lim}=256$, which was used to classify initial condition as strongly chaotic. Figure 8 shows a very good agreement between the maps of both indicators. The maps reveal a complex structure spanned by two MMRs, 6:5 MMR centered around $a_\mathrm{b}\simeq 0.1135$ au, and 7:6 MMR centered around $a_\mathrm{b}\simeq 0.1155$ au. From these two first order resonances emerge an extended overlap zone. We note a large range of REM values spanning 7 orders of magnitude. The border of the dynamical collision zone of the orbits may be clearly seen as a change of shades across the map, which is very close to a thick, gray curve determined by the mutual Hill radius separation from the geometrical collision curve (thick grey

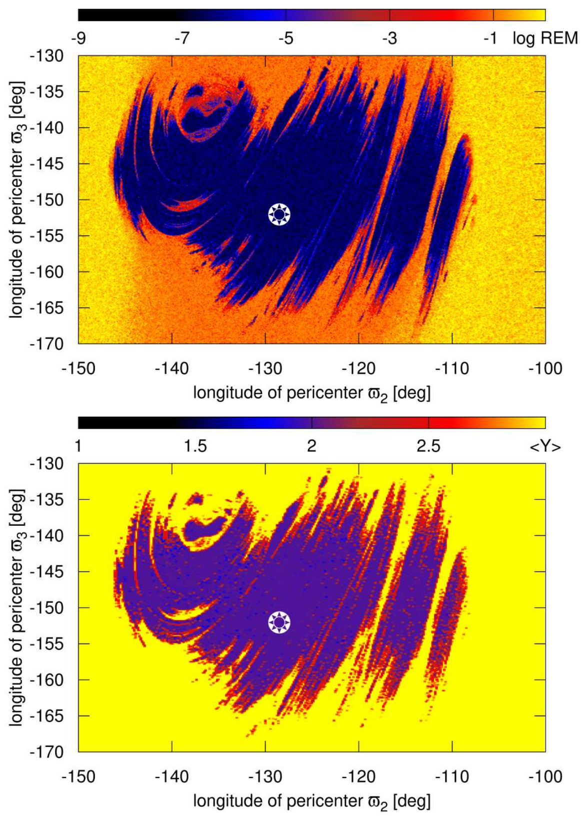

Figure 7. The REM and MEGNO dynamical maps for the Kepler-60 system in the (ϖ_c, ϖ_e)-plane. The initial condition is displayed in Tab. 1 and marked here with the star symbol. Note that grid resolutions are different, 800×600 for REM, and 720×720 for MEGNO. Integration time is 16 kyrs for MEGNO and 32 kyrs for REM.

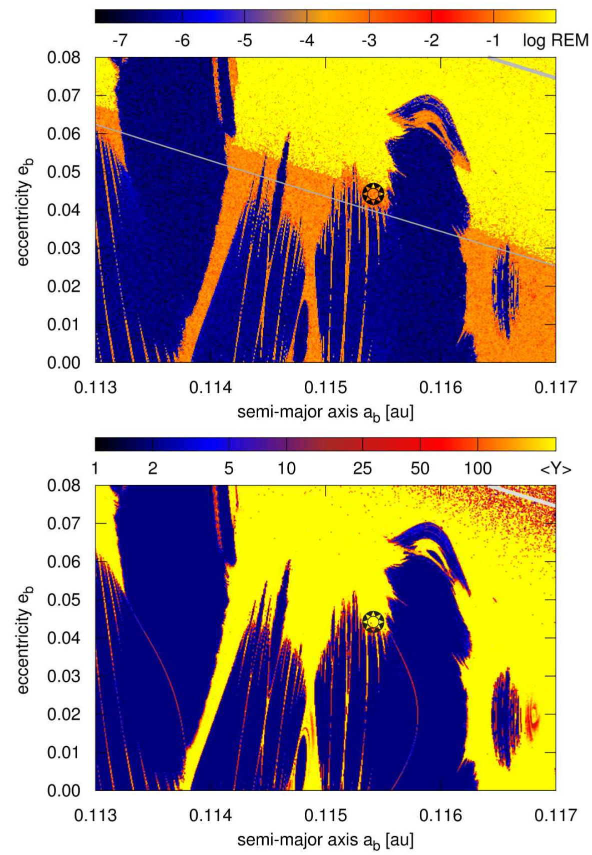

Figure 8. MEGNO and REM comparison for Kepler-36. *Top panel* is for the second order leapfrog-UVC(5) REM map in (a_b, e_b)-plane, forward integration interval is 18 kyrs. *Bottom panel* is for symplectic MEGNO with 4th order $SABA_4$ scheme, time-step 0.5 days and the forward time interval is 36 kyrs. The resolution is 640×480. The star symbol marks the nominal initial condition displayed in Tab. 1. Thick gray curve marks the mutual Hill radius separation of the orbits from the crossing curve.

curve, Fig. 8). All major structures are fully recovered, in spite of the proximity to collisional region.

Yet there are subtle differences between both maps, i.e., a very thin arcs of unstable initial conditions across the 6:5 and 7:5 MMRs, which are present in the MEGNO map, and may be seen as a border of changing shades of blue color (dark grays) in the REM map. They may be attributed to secondary resonances between the resonant and apsidal frequencies of the system, similar to the Kepler-26 case described earlier.

4.6 System 6: stable chaos in 9:7 MMR of Kepler-29?

In Fig. 9 we present the REM and MEGNO maps for Kepler-29 system. The map in the top panel has been obtained (Sect. 3) with the symplectic MEGNO algorithm with $SABA_4$ and a step-size of 0.25 and 0.5 days, respectively. The integration interval is 72 kyrs. The bottom panel shows the REM dynamical map obtained with the same 4th order integrator, and the same total interval of 72 kyrs (2×10^6 outermost orbits). A thin, vertical grey line across the REM map marks the change of the time-step from 0.25 days to 0.5 days. The longer time-step has no impact on the results besides smaller REM (darker shade). The overall shape of the 9:7 MMR is clearly recovered in both maps (Fig. 9), and major structures are the same in a region of moderate eccentricities. This amazingly complex and regular structure of the 9:7 MMR is related to secondary resonances which are characteristic for low-eccentricity systems and appear due to a commensurability of the resonant frequency with the apsidal libration frequency (e.g., Morbidelli 2002).

However, significant differences of the absolute REM values appear in the regions of the central, V-shaped MMR. While MEGNO detects strong, chaotic motions in this part of the MMR, the REM signature is typical for ordered motions. We note that mLCE in the central strip is as large as $\sim 0.02/\mathrm{yr}^{-1}$, given the maximal value of $\langle Y \rangle = 768$ has been reached in 72 kyrs, and we approximate $\mathrm{mLCE} \equiv \lambda = 2\langle Y \rangle$, in accord with Eq. 7.

We confirmed this mysterious discrepancy with the long-term direct integrations for 128 kyrs, as well as with ODEX-based MEGNO algorithm, which did not bring a solution to this apparent paradox. Therefore we used the third fast indicator, the FMFT. We choose time-step of 0.5 days and $N = 2^{22}$ for the same grid of initial conditions as for MEGNO and REM (9). This is equivalent to $T \sim 2 \times 10^5$ outermost periods, hence to typical REM integration time for other KEPLER systems. No signs of geometric instability have been found in the problematic zone, in the sense of a lack of significant variation of the osculating elements and the proper mean motions. Moreover, we found a very close agreement of the REM and FMFT signatures. These maps could be hardly distinguished.

Moreover, the top-right panel in Fig. 9 shows the REM map integrated with the leapfrog-UVC(5) integrator for $\sim 2 \times 9$ kyrs and time-step of 0.25 days only, still revealing the same dynamical structures as in the top-left map for effectively 8 times longer integration time and higher-order schemes.

The FMFT experiment help us to explain the different signatures of REM and MEGNO by the so called "stable chaos" phenomenon. This phenomenon was discovered by Milani & Nobili (1992); Milani et al. (1997) for asteroid motions. It is found to be due to high order MMRs with Jupiter in combination with secular perturbations on the perihelia of the asteroids. While a detailed analysis of the Kepler-29 system is beyond the scope of this paper, it may be a clear evidence of the stable chaos for KEPLER planets involved in low-order MMRs (see also, Deck et al. 2013). This is unusual since large mLCE appear due to secular interactions of relatively low-dimensional, two planets system only. We found the same effect, though much subtle, in Kepler-36 system, as well as in Kepler-26 system.

The results of this experiment are the most clear indication of a possibility of different classification of particular unstable (chaotic) orbits by REM and mLCE, similar to Kepler-26 and Kepler-36 examples. It clearly appears in the regions spanned by MMRs. As shown for the FGL Hamiltonian, and for the restricted three body problem (see the next Section), REM appears as better conserved ("stable") for quasi-regular resonant motions, which decrease (change) the reversibility index α in the t^{α} when compared to non-resonant trajectories, qualitatively equivalent to the Brouwer law n^{α}, where n is the number of time-steps.

Given the results of the Kepler-29 experiment, the REM may be placed between two classes of fast indicators, based on the Lyapunov exponent and spectral methods.

4.7 System 7: Kepler-29 as the restricted three body problem

In the last experiment, we test a modified configuration of the Kepler-29 system (Tab. 1) as the RTBP configuration, which is close to the 9:7 MMR in the N-body model. We made this experiment to illustrate some differences that may appear when REM is computed with different splittings of the same Hamiltonian.

The results are illustrated in Fig. 10. A map in the top panel has been obtained in the framework of the N-body problem (Sect. 3) with the leapfrog-UVC(8) algorithm with step-size 0.25 days and integration time 3.6 kyrs. The bottom panel shows the REM dynamical map obtained with the 4th order Yoshida integrator, and the forward integration interval of 3.6 kyrs (10^5 revolutions of the binary). However, due to particular Hamiltonian splitting (Sect. 3.2), which is "blind" for the planetary character of the model investigated, the step-size has to be as small as 0.0625 d to conserve the energy at $\sim 10^{-8}$ level.

The overall shape of the 9:7 MMR is clearly recovered in both maps, and the major structures are the same. However, significant differences of the absolute REM values appear in the regions of the central, V-shaped MMR, as well as in higher-order MMRs shown as smaller "drops" out of the central structure. The background level of REM for stable orbits of 10^{-7}–10^{-6} can be the basis to identify regular orbits.

The RTBP map derived with the Yoshida scheme exhibits more clear differentiation of regular orbits. We attribute it to a combination of two numerical effects. One is the different sensitivity for stable-resonant and stable-quasiperiodic orbits (we recall the FGL Hamiltonian example). For the Yoshida integrator, there is also a numerical instability of the "drift" (Eq. 14), which effectively means the rotation by angle $2h$. It results in the energy drift (Petit 1998). Indeed, we found that the Yoshida scheme exhibits such a strong, linear energy drift re-inforced by smaller step-sizes. This numerical instability has likely a different impact for the REM index in stable resonant regions and in stable quasi-periodic zones. They are strongly discriminated as dark-blue (dark gray) and light-cyan (light-gray) regions in the bottom REM map in Fig. 10.

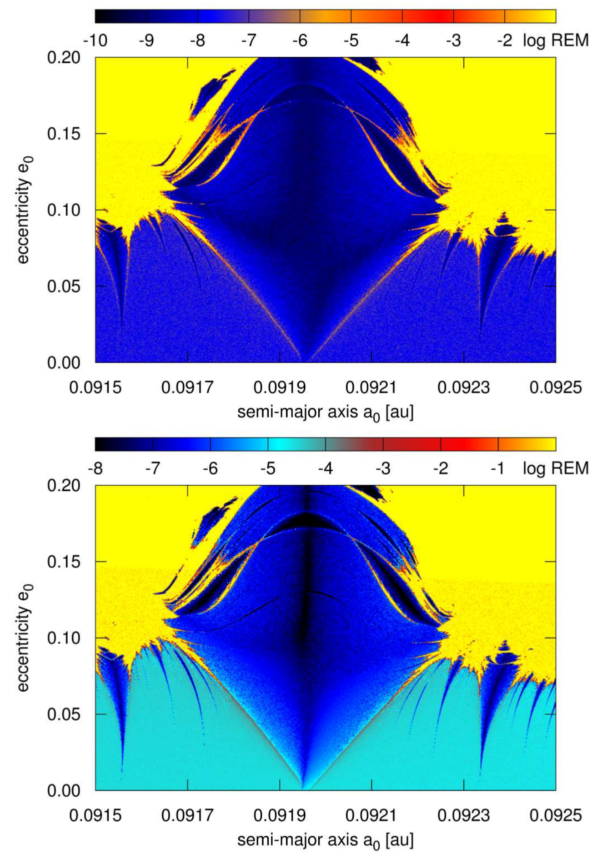

Figure 10. Dynamical REM maps for the N-body and R3BP models (Sect. 3.3 and 3.2) for the Kepler-29-like system in the (a_0, e_0) of the massless planet (Tab. 2). The top panel is the N-body REM map, and the bottom panel the R3BP REM map. In both cases the grid resolution is equal to 900×768 points, and the forward interval of integration is 3.6 kyrs.

Yet the N-body variant of REM outperforms the RTBP model in the CPU overhead. A single initial condition was integrated with the leapfrog-UVC(5) scheme for a 4.4 seconds, while the 4th order Yoshida integrator required ~ 7.7 seconds, though the energy error is worse by 1-2 orders of magnitude.

We conclude the leapfrog-UVC(5) REM algorithm may be used for investigating the dynamical structure of 2-planet KEPLER systems, if they could be described in the framework of RTBP. We also note that the RTBP could be easily generalized with perturbations like primaries oblateness, radiation, and other conservative effects. As far as such perturbed problems could be solved with symplectic and reversible algorithm, REM may be the method of choice, given its straightforward implementation.

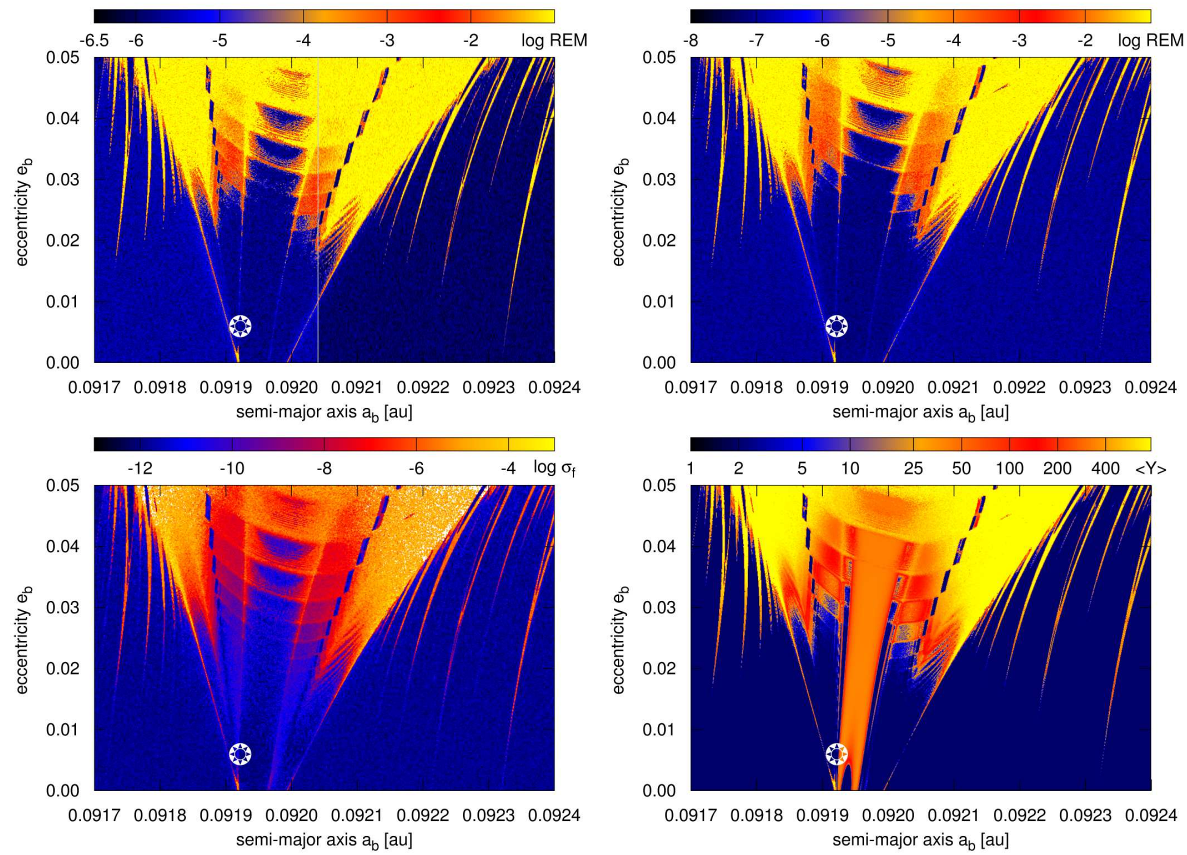

Figure 9. Dynamical maps for Kepler-29 (Tab. 1) in $(a_\mathrm{b}, e_\mathrm{b})$-plane. *Top-left panel* is the N-body REM map, divided for two parts: the left is for SABA$_4$ with time-step $h = 0.25$ d, and the right one is for SABA$_3$ with time-step $h = 0.5$ days, forward integration interval is 2×36 kyrs. *Bottom-right panel* is for symplectic MEGNO map with SABA$_4$ integrator, time-step 0.5 days, integrated for 72 kyrs. *Bottom-left panel* is for the diffusion frequency for the inner planet, the integration spans 2×2^{22} time-steps of 0.5 day. *Top-right panel* is for the REM map with the leapfrog-UVC(5), time-step 0.25 days, and the interval is 2×9 kyrs. The resolution of all grids is equal to 1024×768 points. The star symbol marks the nominal initial condition displayed in Tab. 1.

5 NUMERICAL SETUP AND CPU EFFICIENCY

The most important feature of integrators used to compute the dynamical maps in Sect. 4 is the time-reversibility, closely related to conservation of the first integrals (Hairer et al. 2002). Usually, as much as 10^5–10^6 characteristic periods must be considered when we want to investigate large volumes or the fine structures of the phase-space. Therefore the CPU overhead is the next critical factor for choosing integrations schemes. We focus on low-eccentric planetary systems, when constant time-step is permitted due to relatively small mutual perturbations. We aim to analyze the most relevant integrators features, like the maximal reliable time-step, total integration time and preservation of the first integrals of motion, when used to compute the dynamical maps in Sect. 4. We use the Kepler-26 and Kepler-36 systems as test-bed configurations.

5.1 Keplerian solvers and the leapfrog implementations

The classic "planetary" leapfrog scheme (Hairer et al. 2002), and its derivatives, as the SABA$_n$/SBAB$_n$ schemes (Laskar & Robutel 2001) or Yoshida integrators (Yoshida 1990), is composed of the Keplerian drift, which propagates the system along Keplerian orbits, and a kick, which corresponds to the linear advance of the momenta. This is the genuine (Wisdom & Holman 1991) scheme, known as the mixed-variable symplectic leapfrog. A crucial factor for implementing this algorithm is an accurate and fast solver for propagating the initial conditions at Keplerian orbit. In our implementation, we used Keplerian drift code of Levison & Duncan (1994) in their SWIFT package, which become a de-facto numerical standard. A version of the leapfrog and higher order schemes with the DL drift are postfixed with "-DL" throughout the text. We also used a new, improved Keplerian solver by Wisdom & Hernandez (2015), kindly provided by the authors (J. Wisdom, private communication). This solver is based on the universal variables (Stumpff 1959), yet without Stumpff series. The REM variants with this solver are postfixed by "-UV". Finally, to improve the accuracy of the classical leapfrog integrations, we used symplectic correctors introduced in Wisdom (2006). Our most "sophisticated" leapfrog REM implementation is then leapfrog-UVC(n) algorithm with Wisdom correctors of order $n = 1, 3, 5, 7, 8$.

5.2 Time-reversibility and CPU overhead of SABA$_n$ schemes

Without the round-off errors, a symmetric integrator would be time-reversible independent on the constant step-size (Hairer et al. 2002). When the round-off errors are present, the algorithm introduces certain systematic errors depending on the number of steps.

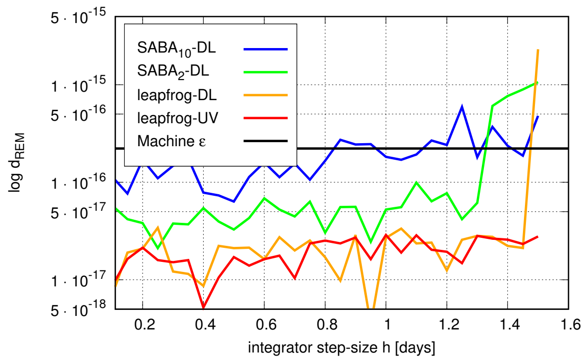

Figure 11. Reversibility test of SABA$_n$ and the canonical leapfrog schemes. The time-reversibility breaks when the time-step is too large.

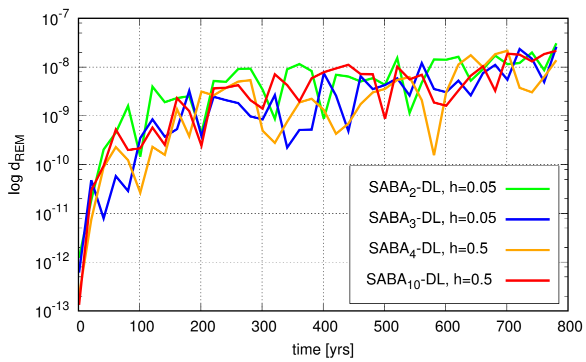

Figure 12. Time-reversibility test of SABA$_n$ schemes for 800 yrs. We choose a stable HD 37124 configuration to test. SABA$_2$, SABA$_3$ outputs are illustrated for the time-step $h = 0.05$ days, and SABA$_4$ and SABA$_1$0 for $h = 0.5$ days. Depending on selected scheme, the energy is preserved with different precision but for all the schemes it does not exceed 10^{-9} in the relative scale.

Therefore the REM outputs may subtly depend on the time-step, Hamiltonian splitting, and total integration time.

Fig. 11 illustrates numerical single-step reversibility for the second order and the 10th-order SABA$_n$ schemes as well as the leapfrogs with DL and UV solvers. In this test, we perform one forward integration time-step h and then the backward one for $-h$. Clearly all schemes are time-reversible up to machine-precision (IEEE floating-point arithmetic, MACH $\sim 2.2 \times 10^{-16}$), as expected, for a wide range of time-steps. In fact, the reversibility is even better than the MACH value, since the calculations were performed on INTEL-architecture CPU with registers of 80 bits.

For a longer forward time interval, equal to 800 yrs and large number of steps, the final REM value for a stable orbit slowly increases with total number of time-steps (Fig. 12), essentially uniformly for different order methods and step-sizes. For this relatively short integration time, REM is preserved to 10^{-7}.

Figure 13 presents the relative CPU overheads for SABA$_n$ schemes for the REM integrations of a stable orbit in the Kepler-26 system. The time-step was changed between 0.1 and 1 days. The forward integration time is fixed to 10 kyrs. For short time-steps ~ 0.1 days, which correspond to $1/170$ of the outermost orbital period (~ 17.25 days), the CPU time would be essentially non-realistic and unacceptable for massive integrations with high-order methods, like SABA$_6$ or SABA$_{10}$. For lower-order SABA$_n$ integra-

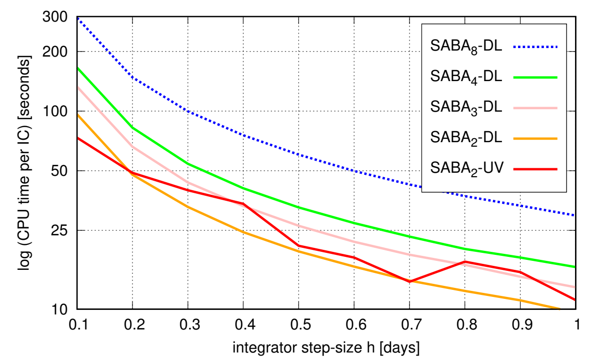

Figure 13. A relative CPU overhead for REM with different SABA$_n$ schemes. The CPU time is expressed in seconds per single initial condition and total integration time of 2×10 kyrs.

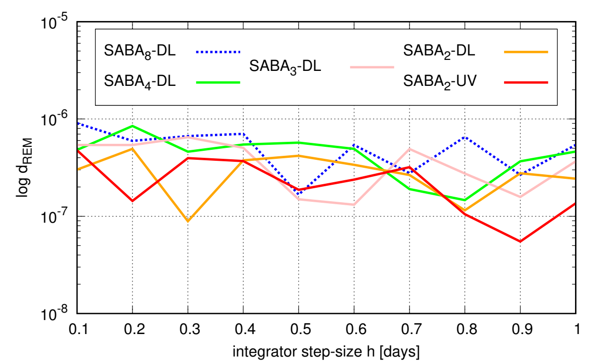

Figure 14. REM outputs for a range of time-steps and total integration time of 2×10 kyrs. A stable configuration of the Kepler-26 planetary system (Tab.1) is tested.

tors, the CPU overhead is still significant, and depends weakly on the Keplerian solvers. We observed some gain of accuracy and performance when using the UV-drift code. At the same time, the reversibility test in Fig. 14 suggest that the REM value depends little on the integrator scheme used for a wide range of time-steps. This could mean that low-order SABA$_n$ algorithms should be preferred for REM calculations to the higher order integrators, provided "a reasonable" relative energy conservation to 10^{-7}–10^{-8} is guaranteed for regular orbits.

5.3 SABA$_n$ vs. the second order leapfrog

The results illustrated in Fig. 12 and close to uniform behavior of REM inspired us to test the second order, classic leapfrog algorithm. Its CPU overheads may be greatly reduced due to concatenating subsequent half-steps. For instance, the sequence drift-kick-drift, once initialized with half-step drift, may be continued by full time-steps drift-kick sequence, reducing the number of the force calls. The integration sequence is finalized with half-step drift, when the end-interval result of the integration is required. This is the REM case. Figure 15 illustrates the REM outputs for a stable configuration in the Kepler-26 system, when integrated for the forward interval of 10 kyrs and different variants of the leapfrog algorithm. The step-size is varied between 0.1 and 1 days, though we warn the reader that $h > 0.5$ may introduce numerical instability

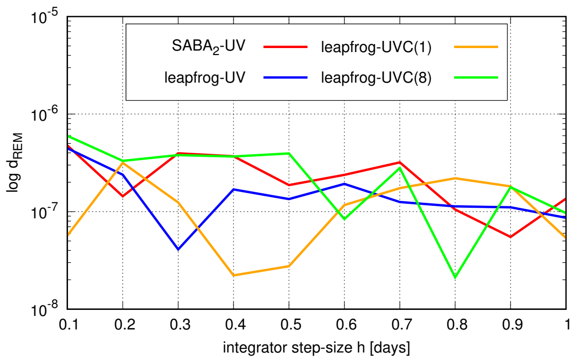

Figure 15. Reversibility test for different leapfrog schemes: leapfrog with the UV drift (dark-gray thin line), also with the UV solver and the Wisdom correctors of first (light-gray thick line) and eight (black thick line) orders. For a reference reference, SABA$_2$ with the UV drift is illustrated (light-gray thin line).

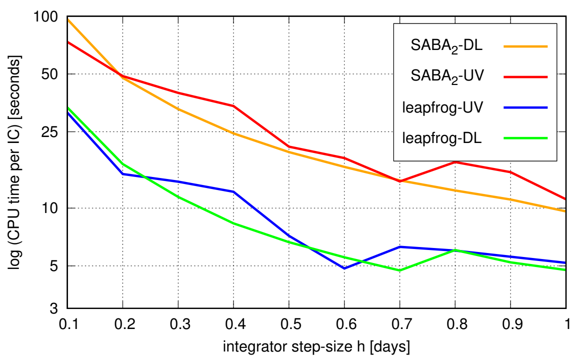

Figure 16. A comparison of REM CPU overhead for variants of the leapfrog: SABA$_2$ with the DL drift (dark thin gray), leapfrog with the DL drift (black thin line), and SABA$_2$ with the UV drift (light gray line), as well as leapfrog with the UV drift (black thick line). Total integration time is 2×10 kyrs.

for chaotic orbits. This test shows that all the methods provide similar REM outputs, though the UV- and UVC(n) algorithms conserve the energy better. We note that REM fluctuations spanning roughly 1 order of magnitude do not have likely any systematic meaning, given a very small statistics of measurements.

However, quite surprising results are provided by the CPU time test. Given the classic leapfrog variants optimized by the concatenation of sub-steps, these schemes systematically outperform SABA$_2$ almost by two-times, independent of the step-size in a reasonable range of $[0.1, 1]$ days. We found that uncorrected leapfrog fails the REM test for shorter time-steps than its corrected variant.

For sufficiently small step-sizes, the corrected leapfrog with Keplerian drift by Wisdom & Hernandez (2015) may be the less CPU demanding REM algorithm, still providing reliable results, as compared to MEGNO computed with high-order SABA integrators, or the non-symplectic Bulirsch-Stoer-Gragg scheme. To illustrate that, in Fig. 17 we computed the mean error of the energy for 10 kyrs of the Kepler-26 system (Tab. 1). We used four variants of the second order leapfrogs. Even for step-sizes as large as 1 day, the mean error of energy is $\sim 10^{-6}$, and with some gain with the symplectic correctors.

Next Fig. 18 is for the energy error computed with the REM

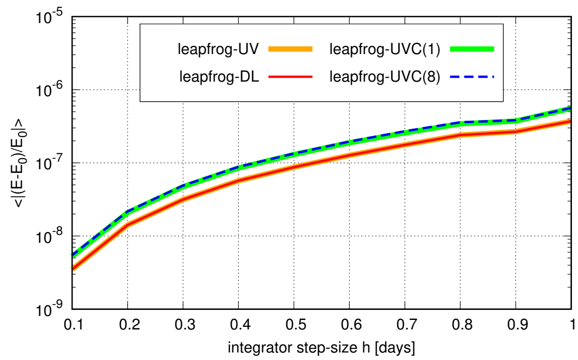

Figure 17. Mean error of the energy for the leapfrog variants tested in this paper. The Kepler-26 initial condition was examined (Tab. 1). Here, leapfrog+DF means the second order leapfrog with (Levison & Duncan 1994) Keplerian drift, leapfrog-UV means the leapfrog with Keplerian drift code by (Wisdom & Hernandez 2015), leapfrog-UVC(n) is for this algorithm and (Wisdom 2006) correctors of the order 1 and 5, respectively.

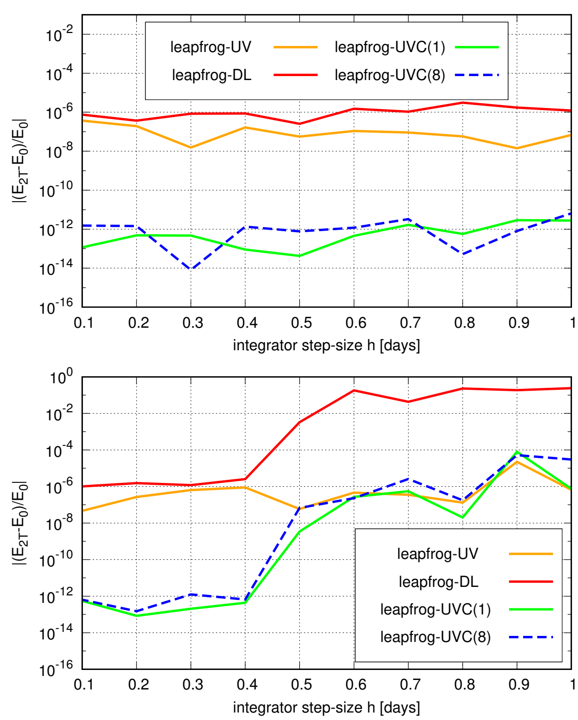

Figure 18. Energy error after integrating the REM value for the leapfrog variants tested in this paper (see caption of the previous figure), for Kepler-26 (*top panel*), and Kepler-29 (*bottom panel*) initial conditions, see Tab. 1.

estimation, i.e., after the interval $t = 2T \equiv T + \| - T\|$, relative to the initial value at $t = 0$, where T is the forward integration time. We tested two systems, Kepler-26 (top panel), and Kepler-29 (bottom panel). For this particular numerical setup, the Wisdom correctors improve the energy conservation by a few orders of magnitude, essentially for zero CPU cost. This certainly improves the REM estimate for regular orbits, due to reducing the deviation introduced by the surrogate Hamiltonian solved by the leapfrog, from the true one. Moreover, the results for Kepler-29 bring a clear warning: too large step-size may cause numerical instability of the Keplerian solvers, as well as diminish the great gain of accuracy provided by the correctors. In fact, our large-scale numerical tests in the previous section for Kepler-29 failed with stepsizes longer than 0.5 days.

Our experiments with KEPLER systems in Tab. 1 show that step-sizes of $\sim 1/40$ of the innermost orbital period provide the optimal conservation of the energy $\sim 10^{-8}$–10^{-9} in the relative scale. However, a fine tuning of the step-size may be required for systems of interest, given their proximity to collision and strongly chaotic regions of motion.

6 CONCLUSIONS

In this paper we propose an application of the fast indicator called REM, based on the time-reversibility of Hamiltonian ODEs, to a particular class of planetary systems. They are characterized by quasi-circular orbits and relatively small mutual perturbations. The REM algorithm has been introduced elsewhere. Our numerical application of REM for planetary systems presented in this paper can be regarded as an extension of the analytic theory for quasi-integrable non-linear symplectic maps.

Besides presenting the theoretical aspects, we show that REM is equivalent to variational algorithms, like mLCE, FLI and MEGNO, provided that dynamical systems of interest may be investigated with symplectic and symmetric numerical algorithms. Such systems span the FGL Hamiltonian exhibiting the Arnold web, the restricted three body problem and a few multiple systems detected by the KEPLER mission. The KEPLER systems are the main target of our analysis, since their eccentricities are damped by the planetary migration, and a low range of eccentricities is typical. Moreover, the KEPLER systems are very compact, and are found in 2-body and 3-body MMRs, forming resonances chains. This leads to rich dynamical behaviours.

Revealing the phase-space structures of these dynamically complex systems is possible thanks to CPU efficient fast indicators. We found that REM may be such an useful numerical technique, particularly for investigating the short-term, resonant dynamics of KEPLER systems. Given its simple implementation, it provides essentially the same results, as much more complex algorithms based on variational equations or the frequency analysis.

We show that REM $\sim 10^{-6}$ for stable orbits, weakly depend on orbital and physical parameters of Kepler-26, Kepler-29, Kepler-36 and Kepler-60 systems, respectively, for the integration intervals as much as $\sim 10^6$ orbital periods of the outermost planet, and maximal eccentricities reaching collisional values. MMR's structures, and stability zones are detected similar with the MEGNO algorithm. However, we also found systematic discrepancies in detecting chaotic orbits within the MMRs. While REM is generally sensitive for determining regular and chaotic motions, it may ignore some subtle chaotic structures with very small diffusion of the fundamental frequencies, as indicated by the FMFT Fourier analysis. Such structures are likely associated with the "stable chaos" phenomenon. Combining REM with MEGNO makes it possible to identify such motions without demanding, direct N-body integrations.

One of the crucial aspects of investigating large volumes of the phase-space is CPU overhead. Though the REM could use any symplectic and time-reversible integration scheme, we found that its most CPU efficient and still reliable implementation may be provided by the classic leapfrog scheme. Its variant with the Keplerian solver based on the universal variable and symplectic correctors exhibits at least 2-times less CPU overhead, as compared to all other symplectic integration algorithms tested in this paper. For weakly perturbed systems, REM may be equally or more CPU efficient than MEGNO and other algorithms in the variational class. This means that high-resolution dynamical maps for time-scales of 10^4–10^5 characteristic periods, which are sufficient to detect major structures of the MMRs, may be computed with single workstation.

Moreover, given the leapfrog efficiency and reliability, the implementation of REM for planetary dynamics requires essentially only essential theory of the Keplerian motion. The REM may be also particularly useful and easy to implement numerical tool for variants of low-dimensional conservative dynamical systems, like the FLG Hamiltonian, restricted three body problem with different perturbations, the Hill problem, galactic potentials, rigid-body and attitude dynamics. The algorithm is also attractive from the didactic point of view.

We believe that the REM could be also implemented with the time-reversibility requirement only, following (Faranda et al. 2012). This could make it possible to apply the algorithm for a wider class of systems, like the regularized three body problem (Dulin & Worhington 2014), and its variants. Besides symplectic symmetric integrators, there are also known symmetric schemes like symmetric Runge-Kutta and collocation methods (e.g., Gauss, LobattoIIIA–IIIB), as well as high-order symmetric composition methods (Hairer et al. 2002). We intent to investigate these integrators for REM analysis in future papers, as well as to provide more arguments for applications of this interesting and appealing algorithm.

7 ACKNOWLEDGEMENTS

This work has been supported by Polish National Science Centre MAESTRO grant DEC-2012/06/A/ST9/00276. K.G. thanks the staff of the Poznań Supercomputer and Network Centre (PCSS, Poland) for their generous and continuous support, and for providing powerful computing resources (grant No. 195).

APPENDIX A: REM, FORWARD AND LYAPUNOV ERRORS ANALYSIS

We briefly introduce here the definition of Lyapunov error (LE), forward error (FE) and reversibility error (RE) for symplectic maps. We refer to symplectic maps since they are invertible and in the linear case the eigenvalues of the matrix and its inverse are the same allowing analytical results to be obtained on the asymptotic equivalence of FE and RE for random perturbations. We first consider a linear map in $\mathbb{R}^{2d}$

$$\boldsymbol{x}_n = A\boldsymbol{x}_{n-1} = A^n\boldsymbol{x}_0 \ , \tag{A1}$$

where A^n is the $n-th$ iteration of A. The linear map is symplectic if A satisfies the condition

$$A\ J\ A^T = A^T\ J\ A = J\ , \qquad J = \begin{pmatrix} 0 & 1 \\ -1 & 0 \end{pmatrix} . \tag{A2}$$

A non linear map is defined to be symplectic

$$\boldsymbol{x}_n = M(\boldsymbol{x}_{n-1})\ , \tag{A3}$$

if its Jacobian matrix $DM(\boldsymbol{x})$ defined by

$$DM_{jk} = \partial M_j/\partial \boldsymbol{x}_k\ , \tag{A4}$$

is symplectic. Above M_j is the j-th element of the symplectic map M, and x_k is the k-th component of the vector $\boldsymbol{x}$. For simplicity from now on we shall refer to symplectic maps of $\mathbb{R}^2$ namely to area preserving maps. We shall analyze in detail the case of integrable maps in normal form. Using action angle variables $\boldsymbol{x} = (\theta, \iota)$ the map reads

$$\begin{aligned} \theta_n &= \theta_{n-1} + \Omega(\iota_{n-1}) \ , \\ \iota_n &= \iota_{n-1} \ . \end{aligned} \tag{A5}$$

The tangent map is constant in this case and reads

$$DM = \begin{pmatrix} 1 & \alpha \\ 0 & 1 \end{pmatrix} \ , \tag{A6}$$

where $\alpha = \Omega'(\iota_n) = \Omega'(\iota_0)$. We consider also the representation of M in Cartesian coordinates $\boldsymbol{x} = (x, y)$

$$\begin{aligned} \boldsymbol{x}_n = R(\Omega)\boldsymbol{x}_{n-1} \ , \qquad & \Omega = \Omega\left(\frac{\|\boldsymbol{x}_{n-1}\|^2}{2}\right) \ . \\ R(\Omega) = \begin{pmatrix} \cos\Omega & \sin\Omega \\ -\sin\Omega & \cos\Omega \end{pmatrix} \ . & \end{aligned} \tag{A7}$$

related to the action angle coordinates by

$$\begin{aligned} y &= \sqrt{2\iota}\cos\theta \ , \\ z &= -\sqrt{2\iota}\sin\theta \ . \end{aligned} \tag{A8}$$

In this second case is important to stress the fact that the tangent map is not constant. The dependence of the rotation frequency on the distance gives a peculiar structure to the tangent map which reads

$$(DM)_{ij} = R_{ij}(\Omega) + R'_{ik}(\Omega)\,\Omega'\,x_j x_k \tag{A9}$$

or using a compact notation

$$DM(\boldsymbol{x}) = R(\Omega) + \Omega' R'(\Omega)\boldsymbol{x}\boldsymbol{x}^T \ . \tag{A10}$$

As a consequence the explicit general calculation of the errors is not trivial. The results we obtain suggest what may be expected from symplectic numerical integration schemes when applied to integrable Hamiltonian systems expressed in Cartesian coordinates.

A1 Lyapunov error

First we define the Lyapunov error showing its relation with the maximal Lyapunov Characteristic Exponent (mLCE). Taking a vector $\boldsymbol{x}_0$ and its displacement in the phase space $\boldsymbol{x}_{\gamma,0}$ defined as

$$\boldsymbol{x}_{\gamma,0} = \boldsymbol{x}_0 + \gamma\boldsymbol{\eta}_0 \ , \tag{A11}$$

where η_0 is an arbitrary versor (unit vector), and γ a small parameter, then the perturbed and unperturbed maps read

$$\begin{aligned} \boldsymbol{x}_n &= M(\boldsymbol{x}_{n-1}) = M^n(\boldsymbol{x}_0) \ , \\ \boldsymbol{x}_{\gamma,n} &= M(\boldsymbol{x}_{\gamma,n-1}) = M^n(\boldsymbol{x}_{\gamma,0}) \ . \end{aligned} \tag{A12}$$

Now, when the parameter γ is very small we can expand the tangent orbit up to first order in γ , at step n, as

$$\boldsymbol{x}_{\gamma,n} = \boldsymbol{x}_n + \gamma\boldsymbol{\eta}_n + O(\gamma^2) \ . \tag{A13}$$

From eq. (A12) and (A13) we obtain the recurrence for $\boldsymbol{\eta}_n$

$$\boldsymbol{\eta}_n = DM(\boldsymbol{x}_{n-1})\boldsymbol{\eta}_{n-1} \ . \tag{A14}$$

The Lyapunov error $d_n^{(L)}$ defined as the norm of the displacement in the phase space is given by

$$d_n^{(L)} = \|\boldsymbol{x}_{\gamma,n} - \boldsymbol{x}_n\| = \gamma\|\boldsymbol{\eta}_n\| + O(\gamma^2) \ . \tag{A15}$$

Now, the definition of the maximal Lyapunov Characteristic Exponent (mLCE) λ reads as

$$\lambda = \lim_{n\to\infty} \frac{1}{n}\,\log\|\boldsymbol{\eta}_n\| = \lim_{n\to\infty} \frac{1}{n}\lim_{\gamma\to 0}\left[\log\left(\frac{d_n^{(L)}}{\gamma}\right)\right] \ . \tag{A16}$$

we then use this general result for different cases.

A2 Lyapunov error for linear canonical maps

The evaluation of LE when the map is linear $M(\boldsymbol{x}) = A\boldsymbol{x}$ and A is in canonical form, is a simple exercise and we quote the results for comparison with the FE and RE errors considered in P16. We notice that the Lyapunov distance $d_n^{(L)}$ is related to the norm of the displacement vector $\boldsymbol{\eta}_n$ by (A15).

A2.1 Parabolic case

The canonical form of the matrix A is

$$A = \begin{pmatrix} 1 & \alpha \\ 0 & 1 \end{pmatrix} \ , \tag{A17}$$

with $\alpha = \Omega'(\beta) > 0$. So that setting $\boldsymbol{\eta}_0 = (\eta_x, \eta_y)$ we have

$$\|\boldsymbol{\eta}_n\| = \left(1 + 2\eta_x\eta_y n\alpha + n^2\alpha^2 n_y^2\right)^{1/2} \ . \tag{A18}$$

The growth is linear unless when $\eta_y = 0$ in that case $\|\boldsymbol{\eta}_n\| = 1$ just as when $\alpha = 0$. The integrable map in action-angle coordinates is amenable to this case: indeed the tangent map of equation (A10) is given by (A17) where $\alpha = \Omega'(\iota_n) = \Omega'(\iota_0)$.

A2.2 Elliptical case

The canonical matrix is the rotation of a fixed angle $A = R(\omega)$. Thus the Euclidean norm is invariant

$$\|\boldsymbol{\eta}_n\| = \|\boldsymbol{\eta}_0\| = 1 \ . \tag{A19}$$

A2.3 Hyperbolic case

For the hyperbolic canonical case the matrix A reads

$$A = \begin{pmatrix} e^{\lambda} & 0 \\ 0 & e^{-\lambda} \end{pmatrix} \ , \tag{A20}$$

and we have

$$\|\boldsymbol{\eta}_n\| = (\eta_x^2 e^{2\lambda n} + \eta_y^2 e^{-2\lambda n}) \ . \tag{A21}$$

This case is of interest because hyperbolic systems have orbits which diverge exponentially with n. The orbits are fully chaotic if phase space is compact. An example is given by the automorphisms of the torus $\mathbb{T}^2$ (linear maps with integer coefficients and unit determinant) such as th Arnold cat map.

A generic linear map $M(\boldsymbol{x}) = B(\boldsymbol{x})$ can always be set in canonical form with a similarity transformation $B = UAU^{-1}$. Since the trace is invariant the elliptic case corresponds to $|\mathrm{Tr}(B)| < 2$, the parabolic case to $\mathrm{Tr}(B) = 2$ and the hyperbolic case to $\mathrm{Tr}(B) > 2$. Denoting with $V = U^T U$ a symmetric positive matrix with unit determinant and $\boldsymbol{\chi}_0 = U^{-1}\boldsymbol{\eta}_0$ we have $\|\boldsymbol{\eta}_n\|^2 = \boldsymbol{\chi}_0 \cdot (A^n)^T VA^n \boldsymbol{\chi}_0$ therefore the result depends on the coefficients a, b, c of the matrix V. In the elliptic case $\|\boldsymbol{\eta}_n\|^2$ has oscillating terms in n, however the asymptotic behavior in n is the same as in the canonical case.

A3 Lyapunov error integrable canonical maps

This section is an extension of the results obtained in P16. We consider here just the canonical maps in the elliptic case which corresponds to the usual integrable case. The tangent map is no longer constant and is given by equation (A10). In order to compute $\boldsymbol{\eta}_n$ by iterating (A14) and using the chain rule we can write

$$DM^n(\boldsymbol{x}_0) = R(n\Omega) + n\Omega' R'(n\Omega)\boldsymbol{x}_0\boldsymbol{x}_0^T \ . \tag{A22}$$

where the index $'$ stay for the derivative over the coordinate. Taking into account that $\|\boldsymbol{x}_n\| = \|\boldsymbol{x}_0\|$ we set $\Omega = \Omega(\|\boldsymbol{x}_0\|^2/2)$ and the same for Ω', thus we obtain

$$\begin{aligned} \|\boldsymbol{\eta}_n\| = \Big(\boldsymbol{\eta}_0 \cdot \Big(R^T(n\Omega) + n\Omega'\boldsymbol{x}_0\boldsymbol{x}_0^T R'^T(n\Omega)\Big)\cdot \\ \cdot \Big(R(n\Omega) + n\Omega' R'(n\Omega)\boldsymbol{x}_0\boldsymbol{x}_0^T\Big)\boldsymbol{\eta}_0\Big)^{1/2} = \\ = \Big(1 + 2n\Omega'\boldsymbol{\eta}_0\cdot\boldsymbol{x}_0\boldsymbol{\eta}_0\cdot J\boldsymbol{x}_0 + n^2(\Omega')^2\boldsymbol{x}_0\cdot\boldsymbol{x}_0\,(\boldsymbol{\eta}_0\cdot\boldsymbol{x}_0)^2\Big)^{1/2} \ , \end{aligned} \tag{A23}$$

where we have taken into account $R^T R' = J$. Comparing this equation with equation (A18) it is possible to observe how, in the integrable non linear case, a linear and quadratic terms in n appear. This is precisely what happens in the parabolic case (see eq. (A17)) which corresponds to the integrable non linear map written in action angle coordinates, whose tangent map is constant. In general the error depends on $\boldsymbol{\eta}_0$ and when it is perpendicular to $\boldsymbol{x}_0$ then $\|\boldsymbol{\eta}_n\| = 1$ as for a constant rotation. The same happens in action angle coordinates when the displacement along the action vanishes ($\eta_y = 0$ in (A15)). This is a characteristic proprieties of Lyapunov methods: the dependence on the initial deviation vector, namely, the choice of initial condition for the tangent map may change the value of mLCE (Barrio et al. (2009)).

A4 Forward error

In this section we introduce the forward error (FE) defined as the displacement of the perturbed orbit $\boldsymbol{x}_{\gamma,n}$ with respect to the exact one, both with the same initial point $\boldsymbol{x}_0$. If the perturbation is due to the round-off the exact map $M(\boldsymbol{x})$ generating the orbit $\boldsymbol{x}_n$ cannot be numerically computed unless we use higher precision. For this reason we propose to use the reversibility error (RE) since for symplectic maps asymptotic equivalence results can be proved for random perturbations, see next section. We start with the definition of the random error vector $\gamma\boldsymbol{\xi}$ with linear independent components and with the proprieties

$$\begin{aligned} \langle\xi_i\rangle &= 0 \ , \\ \langle\xi_i\xi_j\rangle &= \delta_{ij} \ . \end{aligned} \tag{A24}$$

This means that the random vectors have zero mean and unit variance. The amplitude of the noise is γ and for each realization of the random process we have

$$\boldsymbol{x}_{\gamma,n} = M_\gamma(\boldsymbol{x}_{\gamma,n-1}) = M(\boldsymbol{x}_{\gamma,n-1}) + \gamma\boldsymbol{\xi}_n \qquad n \geqslant 1 \ , \tag{A25}$$

with $\boldsymbol{x}_{\gamma,0} = \boldsymbol{x}_0$ meaning that we start from the same point in the phase space. The random vectors chosen at any iteration have independent components

$$\langle(\boldsymbol{\xi}_n)_i\,(\boldsymbol{\xi}_m)_j\rangle = \delta_{m,n}\,\delta_{i,j} \ . \tag{A26}$$

We introduce the stochastic process defined by

$$\boldsymbol{\Xi}_n = \lim_{\gamma\to 0}\frac{\boldsymbol{x}_{\gamma,n} - \boldsymbol{x}_n}{\gamma} = \lim_{\gamma\to 0}\frac{M^n_\gamma(\boldsymbol{x}_0) - M^n(\boldsymbol{x}_0)}{\gamma} \ , \tag{A27}$$

To eliminate fluctuations affecting the FE we consider the following definition of the forward distance

$$d_n^{(F)} = \langle\,\|\boldsymbol{x}_{n,\gamma} - \boldsymbol{x}_n\|^2\,\rangle^{1/2} \ . \tag{A28}$$

The limit of $d_n^{(F)}/\gamma$ is just the mean square deviation of the process $\boldsymbol{\Xi}_n$ whose average is zero. As a consequence from (A28) we obtain $d_n^{(F)} = \gamma\langle\,\|\boldsymbol{\Xi}_n\|^2\,\rangle^{1/2} + O(\gamma^2)$. A recurrence for Ξ_n is easily found observing that from (A27)

$$\boldsymbol{\Xi}_n = \lim_{\gamma\to 0}\frac{\boldsymbol{x}_{\gamma,n} - \boldsymbol{x}_n}{\gamma} = DM(\boldsymbol{x}_{n-1})\boldsymbol{\Xi}_{n-1} + \boldsymbol{\xi}_n \ , \tag{A29}$$

valid for $n \geqslant 1$ with initial condition $\boldsymbol{\Xi}_0 = 0$. The solution is

$$\boldsymbol{\Xi}_n = \sum_{k=1}^{n} DM^{n-k}(\boldsymbol{x}_k)\boldsymbol{\xi}_k \ . \tag{A30}$$

If we perturb the initial condition $\boldsymbol{x}_{\gamma,0} = \boldsymbol{x}_0 + \gamma\,\boldsymbol{\xi}_0$ the recurrence starts with $\boldsymbol{\Xi}_0 = \boldsymbol{\xi}_0$ and (A30) holds with the sum starting from $k = 0$ rather than $k = 1$. In P16 we have shown that

$$\langle\boldsymbol{\Xi}_n\cdot\boldsymbol{\Xi}_n\rangle = \sum_{k=1}^{n}\mathrm{Tr}\left(\mathrm{Tr}\,(DM^{n-k}(\boldsymbol{x}_k))^T DM^{n-k}(\boldsymbol{x}_k)\right) \ . \tag{A31}$$

A4.1 *Forward error for linear canonical maps*

Let the linear map be $M(\boldsymbol{x}) = A\boldsymbol{x}$ where A is the canonical form previously described. Taking (A31) into account with $DM^k = A^k$ the global error is obtained from

$$\langle\boldsymbol{\Xi}_n\cdot\boldsymbol{\Xi}_n\rangle = \sum_{k=0}^{n-1}\mathrm{Tr}\left(A^k\right)^T A^k\right) \ . \tag{A32}$$

A4.2 *Parabolic case*

The matrix A is given by (A17) so that from (A32) we have

$$\langle\boldsymbol{\Xi}_n\cdot\boldsymbol{\Xi}_n\rangle^{1/2} = \left[\sum_{k=0}^{n-1}(2 + \alpha^2k^2)\right]^{1/2} = \frac{\alpha}{\sqrt{3}}n^{3/2}\,O(n^{1/2}) \ . \tag{A33}$$

A4.3 *Elliptical case*

The matrix A is the rotation matrix (see, (A19)) so that

$$\langle\boldsymbol{\Xi}_n\cdot\boldsymbol{\Xi}_n\rangle^{1/2} = \left[\sum_{k=0}^{n-1}2\right]^{1/2} = (2n)^{1/2} \ . \tag{A34}$$

A4.4 *Hyperbolic case*

The matrix A is given by (A20) so that

$$\langle\boldsymbol{\Xi}_n\cdot\boldsymbol{\Xi}_n\rangle^{1/2} = \left[\sum_{k=0}^{n-1}(e^{-2k\lambda} + e^{2k\lambda}\right]^{1/2} = e^{\lambda n} + O(e^{-\lambda n}) \ . \tag{A35}$$

A generic map B is conjugated to its canonical form A by a similarity transformation $B = UAU^{-1}$. In this case the variance of $\boldsymbol{\Xi}_n$ are still given by (A35) where A is replaced by B and $\mathrm{Tr}\left((B^n)^T B^n\right) = \mathrm{Tr}\left(V^{-1}(A^n)^T V A^n\right)$ where $V = U^T U$ is a symmetric positive matrix with unit determinant. Explicit results can be found in P16. Asymptotically in n the behavior of the variance of $\boldsymbol{\Xi}_n$ and consequently $d_n^{(F)}$ is the same as for the corresponding canonical maps.

A5 Forward error for integrable canonical maps

We recall that the canonical form of an integrable map with an elliptic fixed point is given by a rotation matrix $R(\Omega)$ an that according to (A31)

$$DM^{n-k}(\boldsymbol{x}_k) = R((n-k)\Omega) + (n-k)\Omega' R'((n-k)\Omega)\boldsymbol{x}_k\boldsymbol{x}_k^T \ . \quad \text{(A36)}$$

Now proceeding step by step we compute the value $\langle \Xi_n \cdot \Xi_n \rangle$. We first consider the matrix product

$$\begin{aligned} DM^{n-k}(\boldsymbol{x}_k)^T DM^{n-k}(\boldsymbol{x}_k) &= \left(R^T + (n-k)\Omega' \boldsymbol{x}_k\boldsymbol{x}_k^T\,(R')^T\right) \times \\ \times \left(R + (n-k)\Omega' R'\boldsymbol{x}_k\boldsymbol{x}_k^T\right) &= I + (n-k)^2\,\Omega'^2 \boldsymbol{x}_k\boldsymbol{x}_k^T\,R'^T R'\boldsymbol{x}_k\boldsymbol{x}_k^T + \\ + (n-k)\Omega' \left(\boldsymbol{x}_k\boldsymbol{x}_k^T\,R'^T R + R^T R'\boldsymbol{x}_k\boldsymbol{x}_k^T\right) \ . \end{aligned} \quad \text{(A37)}$$

Taking into account that $(R')^T R' = I$ and $R^T R' = J$ plus the additional identities $\mathrm{Tr}\,(J\boldsymbol{x}_k^T\boldsymbol{x}_k)$ and $\mathrm{Tr}\,(\boldsymbol{x}_k^T\boldsymbol{x}_k) = \boldsymbol{x}_k\cdot\boldsymbol{x}_k$ we obtain

$$\mathrm{Tr}\,(\,DM^{n-k}(\boldsymbol{x}_k)^T\,DM^{n-k}(\boldsymbol{x}_k)\,) = 2 + \Omega'^2\,\|\boldsymbol{x}_0\|^4\,(n-k)^2 \ . \quad \text{(A38)}$$

Observing that $\boldsymbol{x}_k\cdot\boldsymbol{x}_k = \boldsymbol{x}_0\cdot\boldsymbol{x}_0$ the final result reads

$$\begin{aligned} \langle \Xi_n \cdot \Xi_n \rangle &= \sum_{k=1}^{n} \mathrm{Tr}\,((DM^{n-k}(\boldsymbol{x}_k)^T\,DM^{n-k}(\boldsymbol{x}_k)) = \\ &= 2n + \Omega'^2\,\|\boldsymbol{x}_0\|^4 \sum_{k=1}^{n}(n-k)^2 \ . \end{aligned} \quad \text{(A39)}$$

The previous result gives the following asymptotic behavior of FE

$$d_n^{(F)} \sim \frac{\gamma}{\sqrt{3}}\,\Omega'\,\|\boldsymbol{x}_0\|^2\,n^{3/2} \ . \quad \text{(A40)}$$

A6 Reversibility error

We consider the reversibility error (RE) for random perturbations presenting cases in which it is asymptotically equivalent to the FE. Here we extend the proof to integrable maps in canonical form. The inverse map at step $n+1$ is affected by a random error $\gamma\boldsymbol{\xi}_{-n-1}$ according to

$$\boldsymbol{x}_{\gamma,-n} = M_\gamma^{-1}\,(\boldsymbol{x}_{\gamma,-n+1}) = M^{-1}(\boldsymbol{x}_{\gamma,-n+1}) + \gamma\,\boldsymbol{\xi}_{-n} \ , \quad \text{(A41)}$$

just as we have considered the direct map, see (A25). The perturbed inverse map is not the inverse of the perturbed map, indeed

$$\begin{aligned} M_\gamma^{-1}(M_\gamma(\boldsymbol{x}_0)) &= M_\gamma^{-1}(M(\boldsymbol{x}_0) + \gamma\,\boldsymbol{\xi}_1) = \\ &= \boldsymbol{x}_0 + \gamma DM^{-1}(\boldsymbol{x}_1)\boldsymbol{\xi}_1 + \gamma\,\boldsymbol{\xi}_{-1} + O(\gamma^2) \ , \end{aligned} \quad \text{(A42)}$$

where both $\boldsymbol{\xi}_1$ e $\boldsymbol{\xi}_{-1}$ are independent stochastic vectors. We introduce the random vector $\Xi_{-m,n}$ such that $\gamma\,\Xi_{-m,n}$ defines the global error after n iterations with M_γ and m iteration with M_γ^{-1} namely

$$\Xi_{-m,n} = \lim_{\gamma\to 0} \frac{M_\gamma^{-m}\,(\boldsymbol{x}_{\gamma,n}) - \boldsymbol{x}_{n-m}}{\gamma} \ . \quad \text{(A43)}$$

Using equation (A26) we define for $m = n$ the displacement between the initial condition in the phase space after n iterations with the perturbed map M_γ and with the perturbed inverse map M_γ^{-1}

$$\Xi_n^{(R)} \equiv \Xi_{-n,n} = \lim_{\gamma\to 0} \frac{M_\gamma^{-n}\,(M_\gamma^n(\boldsymbol{x}_0)) - \boldsymbol{x}_0}{\gamma} \ . \quad \text{(A44)}$$

In order to compute $\Xi_n^{(R)}$ we may use for $\Xi_{m,n}$ the recurrence relation (A29) with respect to m replacing the map M with M^{-1} and taking into account that the initial displacement $\Xi_{0,n}$ is not zero. We obtain the recurrence directly observing that

$$\begin{aligned} \Xi_{-m,n} &= \lim_{\gamma\to 0} \frac{M_\gamma^{-1}(\boldsymbol{x}_{\gamma,n-m+1}) - M^{-1}(x_{n-m+1}) + \gamma\,\boldsymbol{\xi}_{-m}}{\gamma} = \\ &= DM^{-1}(x_{n-m+1})\,\Xi_{-m+1,n} + \boldsymbol{\xi}_{-m} \qquad m \geqslant 1 \ . \end{aligned} \quad \text{(A45)}$$

The initial condition $\Xi_{0,n}$ in this case, according to (A45), is

$$\Xi_{0,n} = \lim_{\gamma\to 0} \frac{\boldsymbol{x}_{\gamma,n} - \boldsymbol{x}_n}{\gamma} = \Xi_n \ . \quad \text{(A46)}$$

The solution is the same as for the forward error with a non vanishing initial condition namely

$$\Xi_{-m,n} = DM^{-m}(\boldsymbol{x}_n)\Xi_n + \sum_{k=1}^{m} DM^{-(m-k)}(\boldsymbol{x}_{n-k})\boldsymbol{\xi}_{-k} \ . \quad \text{(A47)}$$

The stochastic process related to the reversibility error is

$$\Xi_n^{(R)} = \Xi_{-n,n} = DM^{-n}(\boldsymbol{x}_n)\Xi_n + \sum_{k=1}^{n} DM^{-(n-k)}(\boldsymbol{x}_{n-k})\boldsymbol{\xi}_{-k} \ . \quad \text{(A48)}$$

This brings to the follow definition of the reversibility distance

$$d_n^{(R)} = \langle \left\| M_\gamma^{-n}(M_\gamma^n(\boldsymbol{x}_0)) - \boldsymbol{x}_0 \right\|^2 \rangle^{1/2} \ , \quad \text{(A49)}$$

which is related to the mean square deviation of the reversibility error $\Xi_n^{(R)}$ by $d_n^{(R)} = \gamma\langle \left\|\Xi_n^{(R)}\right\|^2\rangle^{1/2} + O(\gamma^2)$ where

$$\begin{aligned} \langle \Xi_n^{(R)} \cdot \Xi_n^{(R)} \rangle &= \sum_{k=1}^{n} \mathrm{Tr}\,\left((DM^{-(n-k)}(\boldsymbol{x}_{n-k}))^T DM^{-(n-k)}(\boldsymbol{x}_{n-k}) \right) + \\ &+ \sum_{k=1}^{n} \mathrm{Tr}\,\left((DM^{-n}(\boldsymbol{x}_n)DM^{n-k}(\boldsymbol{x}_k))^T DM^{-n}(\boldsymbol{x}_n)DM^{n-k}(\boldsymbol{x}_k) \right) \ . \end{aligned} \quad \text{(A50)}$$

A7 Reversibility error for linear canonical maps

Letting the map be $M(\boldsymbol{x}) = A\boldsymbol{x}$ where A is a real matrix in canonical form, the process $\Xi_n^{(R)}$ becomes

$$\Xi_n^{(R)} = \sum_{k=1}^{n} A^{-k}\boldsymbol{\xi}_k + \sum_{k=1}^{n} A^{-(n-k)}\boldsymbol{\xi}_{-k} \ . \quad \text{(A51)}$$

and its variance is

$$\begin{aligned} \langle \|\Xi_n^{(R)}\|^2 \rangle &= \sum_{k=1}^{n} \mathrm{Tr}\,(\,(A^{-k})^T A^{-k}\,) + \sum_{k=0}^{n-1} \mathrm{Tr}\,(\,(A^{-k})^T A^{-k}\,) = \\ &= 2\sum_{k=0}^{n-1} \mathrm{Tr}\,(\,(A^{-k})^T A^{-k}\,) + \mathrm{Tr}\,(\,(A^{-n})^T A^{-n} - I\,) \ . \end{aligned} \quad \text{(A52)}$$

A7.1 *Parabolic case*

$$\langle \|\Xi_n^{(R)}\|^2 \rangle^{1/2} = \left(2\langle \|\Xi_n\|^2 \rangle + n^2\alpha^2 \right)^{1/2} \ . \quad \text{(A53)}$$

A7.2 *Elliptic case*

$$\langle \|\Xi_n^{(R)}\|^2 \rangle^{1/2} = \left(2\langle \|\Xi_n\|^2 \rangle \right)^{1/2} \ . \quad \text{(A54)}$$

A7.3 Hyperbolic case

$$\langle \|\boldsymbol{\Xi}_n^{(R)}\|^2\rangle^{1/2} = \Big(2\langle\|\boldsymbol{\Xi}_n\|^2\rangle + e^{2\lambda n} + e^{-2\lambda n} - 2\Big)^{1/2} . \tag{A55}$$

The forward and reversibility errors are asymptotically proportional one with the other, and at the leading order in n and first order in γ.

A8 Reversibility error for canonical integrable maps

In order to evaluate the mean square deviation of $\boldsymbol{\Xi}_n^{(R)}$ for an integrable map in canonical (normal) form (A9) we use (A52) where $DM^k(\boldsymbol{x})$ is given by (A37). If we take into account that $R^{-k}(\Omega) = R(-k\Omega)$ then the first sum in the r.h.s. of (A52) is the same as for the FE, namely

$$\begin{aligned} &\sum_{k=1}^{n} \mathrm{Tr}\,\Big((DM^{-(n-k)}(\boldsymbol{x}_{n-k}))^T DM^{-(n-k)}(\boldsymbol{x}_{n-k}) \Big) = \\ &\qquad = 2n + \Omega'^2\,\|\boldsymbol{x}_0\|^2 \sum_{k=1}^{n} (n-k)^2 . \end{aligned} \tag{A56}$$

To evaluate the second sum in the r.h.s. of (A52) we first consider a single term contributing to it

$$\begin{aligned} &DM^{-n}(\boldsymbol{x}_n) DM^{n-k}(\boldsymbol{x}_k) = \Big(R(-n\Omega) - n\Omega'\,R'(-n\Omega)\boldsymbol{x}_n\boldsymbol{x}_n^T\Big)\cdot \\ &\cdot\Big(R((n-k)\Omega) + (n-k)\Omega' R'((n-k)\Omega)\boldsymbol{x}_k\boldsymbol{x}_k^T\Big) = \\ &= R(-k\Omega) + (n-k)\Omega'\,R(-n\Omega)\,R'((n-k)\Omega)\boldsymbol{x}_k\boldsymbol{x}_k^T - \\ &- n\Omega'\,R'(-n\Omega)\boldsymbol{x}_n\boldsymbol{x}_n^T\,R((n-k)\Omega) - \\ &- n(n-k)\Omega'^2\,R'(-n\Omega)\boldsymbol{x}_n\boldsymbol{x}_n^T\,R'((n-k)\Omega)\boldsymbol{x}_k\boldsymbol{x}_k^T . \end{aligned} \tag{A57}$$

To evaluate equation (A57) and the trace of the matrix times its transpose, we use the the following relations

$$\begin{aligned} &R^T(\alpha)R'(\alpha) = R(-\alpha)R'(\alpha) = J \qquad R'^T(\alpha)R(\alpha) = J^T = -J \\ &R'(\alpha)R^T(\alpha) = R'(\alpha)R(-\alpha) = J \qquad R(\alpha)R'^T(\alpha) = J^T = -J \\ &R(-\alpha)JR(\alpha) = J . \end{aligned} \tag{A58}$$

where J is the matrix defined by (A2) with $l = 1$. We show first the last term in the r.h.s. of (A57) vanishes

$$\begin{aligned} &\boldsymbol{x}_n^T\,R'((n-k)\Omega)\boldsymbol{x}_k = \boldsymbol{x}_0^T R(-n\Omega)R'((n-k)\Omega)R(k\Omega)\boldsymbol{x}_0 = \\ &= \boldsymbol{x}_0^T R(-k\Omega)\,R(-(n-k)\Omega)R'((n-k)\Omega)R(k\Omega)\boldsymbol{x}_0 = \\ &= \boldsymbol{x}_0^T R(-k\Omega)\,J\,R(k\Omega)\boldsymbol{x}_0 = \boldsymbol{x}_0^T\,J\boldsymbol{x}_0 = 0 , \end{aligned} \tag{A59}$$

since the matrix J is antisymmetric.

The next step is to evaluate the following product where we introduce the following notation $R_k = R(k\Omega)$ and $R'_k = R'(k\Omega)$

$$\begin{aligned} &(DM^{-n}(\boldsymbol{x}_n)DM^{n-k}(\boldsymbol{x}_k))^T\,DM^{-n}(\boldsymbol{x}_n)DM^{n-k}(\boldsymbol{x}_k) = \\ &= \Big(R_k + (n-k)\Omega'\,\boldsymbol{x}_k\boldsymbol{x}_k^T\,R'^T_{n-k}R_n - n\Omega'\,R_{-(n-k)}\boldsymbol{x}_n\boldsymbol{x}_n^T\,R'^T_{-n}\Big)\times \\ &\times\Big(R_{-k} + (n-k)\Omega'\,R_{-n}\,R'_{n-k}\boldsymbol{x}_k\boldsymbol{x}_k^T - n\Omega'\,R'_{-n}\boldsymbol{x}_n\boldsymbol{x}_n^T\,R_{n-k}\Big) . \end{aligned} \tag{A60}$$

Developing the product in (A60) we have 9 terms: the identity, four terms linear in Ω' whose trace is zero and four terms quadratic in Ω' which are all equal. Indeed the trace of terms linear in Ω' is

$$\begin{aligned} &\mathrm{Tr}\,\Big(R_k R_{-n}\,R'_{n-k}\boldsymbol{x}_k\boldsymbol{x}_k^T\Big) = \mathrm{Tr}\,\Big(J\boldsymbol{x}_k\boldsymbol{x}_k^T\Big) = 0 , \\ &\mathrm{Tr}\,\Big(R_k\,R'_{-n}\boldsymbol{x}_n\boldsymbol{x}_n^T\,R_{n-k}\Big) = \mathrm{Tr}\,\Big(J\boldsymbol{x}_n\boldsymbol{x}_n^T\Big) = 0 , \\ &\mathrm{Tr}\,\Big(R_{-n}\,R'_{n-k}\boldsymbol{x}_k\boldsymbol{x}_k^T\,R_{-k}\Big) = \mathrm{Tr}\,\Big(J\boldsymbol{x}_k\boldsymbol{x}_k^T\Big) = 0 , \\ &\mathrm{Tr}\,\Big(R_{-(n-k)}\boldsymbol{x}_n\boldsymbol{x}_n^T\,R'^T_{-n}R_{-k}\Big) = \mathrm{Tr}\,\Big(\boldsymbol{x}_n\boldsymbol{x}_n^T J\Big) = 0 , \end{aligned} \tag{A61}$$

where we have systematically used the property $\mathrm{Tr}\,(AB) = \mathrm{Tr}\,(BA)$. The trace of the first term quadratic in Ω' is given by $(n-k)^2\Omega'^2$ times

$$\begin{aligned} &\mathrm{Tr}\,\Big(\boldsymbol{x}_k\boldsymbol{x}_k^T\,R'^T_{n-k}R_n\,R_{-n}\,R'_{n-k}\boldsymbol{x}_k\boldsymbol{x}_k^T\Big) = \\ &= \mathrm{Tr}\,\Big(\boldsymbol{x}_k\boldsymbol{x}_k^T\,\boldsymbol{x}_k\boldsymbol{x}_k^T\Big) = (\boldsymbol{x}_k\cdot\boldsymbol{x}_k)^2 = \|\boldsymbol{x}_0\|^4 , \end{aligned} \tag{A62}$$

where we have used $R'^T(\alpha)R'(\alpha) = I$. The trace of the second quadratic in Ω' is given by $-(n-k)n\Omega'^2$ times

$$\begin{aligned} &\mathrm{Tr}\,\Big(\boldsymbol{x}_k\boldsymbol{x}_k^T\,R'^T_{n-k}R_n\,R'_{-n}\boldsymbol{x}_n\boldsymbol{x}_n^T\,R_{n-k}\Big) = \\ &= \mathrm{Tr}\,\Big(\boldsymbol{x}_k\boldsymbol{x}_k\,R'^T_{n-k}R_{n-k}\,R_k\,R'_{-n}\,R_n\,R_{-k}\boldsymbol{x}_k\boldsymbol{x}_k\Big) = \\ &= \mathrm{Tr}\,(\boldsymbol{x}_k\boldsymbol{x}_k\,(-J)\,R_k\,J, R_{-k}\boldsymbol{x}_k\boldsymbol{x}_k) = -\|\boldsymbol{x}_0\|^4 . \end{aligned} \tag{A63}$$

The trace of the third quadratic in Ω' is $-(n-k)n\Omega'^2$ times

$$\begin{aligned} &\mathrm{Tr}\,\Big(R_{-(n-k)}\boldsymbol{x}_n\boldsymbol{x}_n^T\,R'^T_{-n}R_{-n}\,R'_{n-k}\boldsymbol{x}_k\boldsymbol{x}_k^T\Big) = \\ &= \mathrm{Tr}\,\Big(\boldsymbol{x}_k\boldsymbol{x}_0\,R_{-n}\,R'^T_{-n}\,R_{-k}\,R_{k-n}\,R'_{n-k}\,R_k\boldsymbol{x}_0\boldsymbol{x}_k^T\Big) = \\ &= \mathrm{Tr}\,\Big(\boldsymbol{x}_k\boldsymbol{x}_0\,(-J)\,R_{-k}\,J\,R_k\boldsymbol{x}_0\boldsymbol{x}_k^T\Big) = -\|\boldsymbol{x}_0\|^4 . \end{aligned} \tag{A64}$$

The trace of the fourth quadratic term in Ω' is $n^2\Omega'^2$ times

$$\begin{aligned} &\mathrm{Tr}\,\Big(R_{-(n-k)}\boldsymbol{x}_n\boldsymbol{x}_n^T\,R'^T_{-n}\,R'_{-n}\boldsymbol{x}_n\boldsymbol{x}_n^T\,R_{n-k}\Big) = \\ &= \mathrm{Tr}\,\Big(R_{-(n-k)}\boldsymbol{x}_n\boldsymbol{x}_n^T\,\boldsymbol{x}_n\boldsymbol{x}_n^T\,R_{n-k}\Big) = \|\boldsymbol{x}_0\|^4 , \end{aligned} \tag{A65}$$

again taking into account $R'^T(\alpha)\,R(\alpha) = I$.

Collecting all the four terms we obtain

$$\begin{aligned} &\mathrm{Tr}\,\Big((DM^{-n}(\boldsymbol{x}_n)DM^{n-k}(\boldsymbol{x}_k))^T\,DM^{-n}(\boldsymbol{x}_n)DM^{n-k}(\boldsymbol{x}_k)\Big) = \\ &= (\Omega')^2\,\|\boldsymbol{x}_0\|^4\,\Big(n^2 + 2(n-k) + (n-k)^2)\Big) = \\ &= (\Omega')^2\,\|\boldsymbol{x}_0\|^4\,(2n-k)^2 . \end{aligned} \tag{A66}$$

Adding the contribution of equation (A57) the final result for the

$$\begin{aligned} \langle\boldsymbol{\Xi}_n^{(R)}\cdot\boldsymbol{\Xi}_n^{(R)}\rangle &= 2n + (\Omega')^2\,\|\boldsymbol{x}_0\|^4\,\Bigg[\sum_{k=1}^{n}(n-k)^2 + \sum_{k=1}^{n}(2n-k)^2\Bigg] = \\ &= 2n + (\Omega')^2\,\|\boldsymbol{x}_0\|^4 \sum_{k=1}^{2n-1} k^2 . \end{aligned} \tag{A67}$$

The reversibility distance $d_n^{(R)}$ has the following asymptotic expression

$$d_n^{(R)} \sim \frac{\gamma}{\sqrt{3}}\,|\Omega'|\,\|\boldsymbol{x}_0\|^2\,(2n)^{3/2} + O(\gamma^2) + O(\gamma n^{1/2}) , \tag{A68}$$

which is the same as the forward error where n is replaced by $2n$.

REFERENCES

Aarseth S. J., Anosova J. P., Orlov V. V., Szebehely V. G., 1994, Celestial Mechanics and Dynamical Astronomy, 58, 1
Arnold V. I., 1963, Russian Mathematical Surveys, 18, 9
Baluev R. V., 2008, Celestial Mechanics and Dynamical Astronomy, 102, 297
Barrio R., Borczyk W., Breiter S., 2009, Chaos Solitons and Fractals, 40, 1697
Benettin G., Galgani L., Giorgilli A., Strelcyn J.-M., 1980, Meccanica, 15, 9
Chambers J. E., 1999, MNRAS, 304, 793
Chambers J. E., Wetherill G. W., Boss A. P., 1996, Icarus, 119, 261
Charbonneau P., 1995, ApJS, 101, 309
Chatterjee S., Ford E. B., Matsumura S., Rasio F. A., 2008, ApJ, 686, 580
Chirikov B. V., 1979, Physics Reports, 52, 263
Cincotta P. M., Giordano C. M., Simó C., 2003, Physica D Nonlinear Phenomena, 182, 151
Cincotta P. M., Simó C., 2000, A&AS, 147, 205
Couetdic J., Laskar J., Correia A. C. M., Mayor M., Udry S., 2010, A&A, 519, A10
Deck K. M., Agol E., 2016, ApJ, 821, 96
Deck K. M., Holman M. J., Agol E., Carter J. A., Lissauer J. J., Ragozzine D., Winn J. N., 2012, ApJL, 755, L21
Deck K. M., Payne M., Holman M. J., 2013, ApJ, 774, 129
Dulin H. R., Worhington J., 2014, Physica D, 276, 12
Fabrycky et al. 2012, ApJ, 750, 114
Faranda D., Mestre M. F., Turchetti G., 2012, International Journal of Bifurcation and Chaos, 22, 1250215
Froeschlé C., Guzzo M., Lega E., 2000, Science, 289, 2108
Froeschlé C., Guzzo M., Lega E., 2005, Celestial Mechanics and Dynamical Astronomy, 92, 243
Froeschlé C., Lega E., Gonczi R., 1997, Celestial Mechanics and Dynamical Astronomy, 67, 41
Goździewski K., Breiter S., Borczyk W., 2008, MNRAS, 383, 989
Goździewski K., Migaszewski C., 2014, MNRAS, 440, 3140
Goździewski K., Migaszewski C., Panichi F., Szuszkiewicz E., 2016, MNRAS, 455, L104
Goździewski K., Słonina M., Migaszewski C., Rozenkiewicz A., 2013, MNRAS, 430, 533
Guzzo M., 2005, Icarus, 174, 273
Guzzo M., Knežević Z., Milani A., 2002, Celestial Mechanics and Dynamical Astronomy, 83, 121
Hadden S., Lithwick Y., 2015, ArXiv e-prints
Hairer E., Wanner G., Lubich L., 2002, Geometric Numerical Integration: Structure-Preserving Algorithms for Ordinary Differential Equations, 2nd ed edn. Springer Series in Computational Mathematics 31, Springer Berlin Heidelberg
Ito T., Tanikawa K., 2002, MNRAS, 336, 483
Jontof-Hutter D., Ford E. B., Rowe J. F., Lissauer J. J., Fabrycky D. C., Van Laerhoven C., Agol E., Deck K. M., Holczer T., Mazeh T., 2016, ApJ, 820, 39
Kolmogorov A. N., 1954, Dokl. akad. nauk SSSR, 98, 527
Laskar J., 1990, Icarus, 88, 266
Laskar J., Gastineau M., 2009, Nature, 459, 817
Laskar J., Quinn T., Tremaine S., 1992, Icarus, 95, 148
Laskar J., Robutel P., 2001, Celestial Mechanics and Dynamical Astronomy, 80, 39
Lehto H. J., Kotiranta S., Valtonen M. J., Heinämäki P., Mikkola S., Chernin A. D., 2008, MNRAS, 388, 965
Levison H. F., Duncan M. J., 1994, Icarus, 108, 18
Marois C., Zuckerman B., Konopacky Q. M., Macintosh B., Barman T., 2010, Nature, 468, 1080
Mestre M. F., Cincotta P. M., Giordano C. M., 2011, MNRAS, 414, L100
Michtchenko T. A., Ferraz-Mello S., 2001, AJ, 122, 474
Mikkola S., Innanen K., 1999, Celestial Mechanics and Dynamical Astronomy, 74, 59
Milani A., Nobili A. M., 1992, Nature, 357, 569
Milani A., Nobili A. M., Knežević Z., 1997, Icarus, 125, 13
Mills S. M., Fabrycky D. C., Migaszewski C., Ford E. B., Petigura E., Isaacson H., 2016, Nature, 533, 509
Morbidelli A., 2002, Modern celestial mechanics : aspects of solar system dynamics
Morbidelli A., Giorgilli A., 1995, Journal of Statistical Physics, 78, 1607
Moser J., 1958, Communications on Pure and Applied Mathematics, 11, 81
Panichi F., Ciotti L., Turchetti G., 2016 Vol. 35, Fidelity and Reversibility in the Restricted Three Body Problem. pp 53–68
Petit J.-M., 1998, Celestial Mechanics and Dynamical Astronomy, 70, 1
Quillen A. C., 2011, MNRAS, 418, 1043
Ramm D. J., Nelson B. E., Endl M., Hearnshaw J. B., Wittenmyer R. A., Gunn F., Bergmann C., Kilmartin P., Brogt E., 2016, ArXiv e-prints
Robutel P., Laskar J., 2001, Icarus, 152, 4
Rowe J. F., Coughlin J. L., Antoci V., Barclay T., Batalha N. M., Borucki W. J., Burke C. J., et al. 2015, ApJS, 217, 16
Sato B., Wang L., Liu Y.-J., Zhao G., Omiya M., Harakawa H., Nagasawa M., Wittenmyer R. A., et al. 2016, ApJ, 819, 59
Šidlichovský M., Nesvorný D., 1996, Celestial Mechanics and Dynamical Astronomy, 65, 137
Skokos C., Manos T., 2014, ArXiv e-prints
Słonina M., Goździewski K., Migaszewski C., 2015, New Astronomy, 34, 98
Steffen J. H., Fabrycky D. C., Ford E. B., Carter J. A., Désert J.-M., Fressin F., Holman M. J., Lissauer J. J., et al. 2012, MNRAS, 421, 2342
Stumpff K., 1959, Himmelsmechanik.
Turchetti G., Vaienti S., Zanlungo F., 2010a, Physica A Statistical Mechanics and its Applications, 389, 4994
Turchetti G., Vaienti S., Zanlungo F., 2010b, EPL (Europhysics Letters), 89, 40006
Vogt S. S., Butler R. P., Marcy G. W., Fischer D. A., Henry G. W., Laughlin G., Wright J. T., Johnson J. A., 2005, ApJ, 632, 638
Wisdom J., 1983, Icarus, 56, 51
Wisdom J., 2006, AJ, 131, 2294
Wisdom J., Hernandez D. M., 2015, MNRAS, 453, 3015
Wisdom J., Holman M., 1991, AJ, 102, 1528
Wright J. T., Veras D., Ford E. B., Johnson J. A., Marcy G. W., Howard A. W., Isaacson H., Fischer D. A., Spronck J., Anderson J., Valenti J., 2011, ApJ, 730, 93
Yoshida H., 1990, Physics Letters A, 150, 262